

## Small-scale structure traced by neutral hydrogen absorption in the direction of multiple-component radio continuum sources

DANIEL R. RYBARCZYK,<sup>1</sup> SNEZANA STANIMIROVIĆ,<sup>1</sup> ELLEN G. ZWEIBEL,<sup>1,2</sup> CLAIRE E. MURRAY,<sup>3</sup> JOHN M. DICKEY,<sup>4</sup>  
BRIAN BABLER,<sup>1</sup> AND CARL HEILES<sup>5</sup>

<sup>1</sup>*Department of Astronomy, University of Wisconsin–Madison, Madison, WI 53706, USA*

<sup>2</sup>*Department of Physics, University of Wisconsin–Madison, Madison, WI 53706, USA*

<sup>3</sup>*Department of Physics & Astronomy, Johns Hopkins University, Baltimore, MD 21218, USA*

<sup>4</sup>*School of Natural Sciences, University of Tasmania, Hobart, TAS 7001, Australia*

<sup>5</sup>*Department of Astronomy, University of California, Berkeley, CA 94720-3411, USA*

(Received February 20, 2020; Revised March 24, 2020; Accepted March 25, 2020)

Submitted to ApJ

### ABSTRACT

We have studied the small scale distribution of atomic hydrogen (HI) using 21-cm absorption spectra against multiple-component background radio continuum sources from the 21-SPONGE survey and the Millennium Arecibo Absorption Line Survey. We have found  $> 5\sigma$  optical depth variations at a level of  $\sim 0.03$ – $0.5$  between 13 out of 14 adjacent sightlines separated by a few arcseconds to a few arcminutes, suggesting the presence of neutral structures on spatial scales from a few to thousands of AU (which we refer to as tiny scale atomic structure, TSAS). The optical depth variations are strongest in directions where the HI column density and the fraction of HI in the cold neutral medium (CNM) are highest, which tend to be at low Galactic latitudes. By measuring changes in the properties of Gaussian components fitted to the absorption spectra, we find that changes in both the peak optical depth and the linewidth of TSAS absorption features contribute to the observed optical depth variations, while changes in the central velocity do not appear to strongly impact the observed variations. Both thermal and turbulent motions contribute appreciably to the linewidths, but the turbulence does not appear strong enough to confine overpressured TSAS. In a majority of cases, the TSAS column densities are sufficiently high that these structures can radiatively cool fast enough to maintain thermal equilibrium with their surroundings, even if they are overpressured. We also find that a majority of TSAS is associated with the CNM. For TSAS in the direction of the Taurus molecular cloud and the local Leo cold cloud, we estimate densities over an order of magnitude higher than typical CNM densities.

### 1. INTRODUCTION

For over 40 years, high-resolution absorption measurements of the 21-cm line of atomic hydrogen (HI) have revealed significant non-uniform structure of interstellar gas on angular scales  $\lesssim 1'$ . This has traditionally been interpreted as evidence for small, over-dense, overpressured HI structures—the so-called tiny scale atomic structure (TSAS; Heiles 1997, 2000; Stanimirović & Zweibel 2018, hereafter SZ18). Under a simple geometric assumption, these structures have densities and pressures several orders of magnitude higher than either the cold neutral medium (CNM) or warm neutral medium (WNM), the two stable thermal phases that underlie most models of the Galactic neutral interstellar medium (ISM).

While the origin of TSAS is still an open question, such structures have been proposed to enhance molecu-

lar abundances (Smith et al. 2013), increase heating of the neutral ISM (SZ18), mark sites of turbulent dissipation (Zweibel 2006), or possibly represent ablated stellar or planetary material (Ray & Loeb 2017). Constraining observationally physical properties of TSAS is essential for understanding its origin and role in the ISM.

One way TSAS is observed is by constructing high resolution optical depth images against extended radio continuum sources, typically using very long baseline interferometry (VLBI), where the pixel-to-pixel variations reveal TSAS (e.g., Diamond et al. 1989; Deshpande et al. 2000; Faison & Goss 2001; Brogan et al. 2005; Goss et al. 2008; Lazio et al. 2009; Roy et al. 2012). In addition to spatial variations, the temporal variations of HI absorption measured against extragalactic radio continuum sources and Galactic pulsars (whose transverse velocities are  $\sim 10$ – $100$  AU yr<sup>-1</sup>) have been used to probe

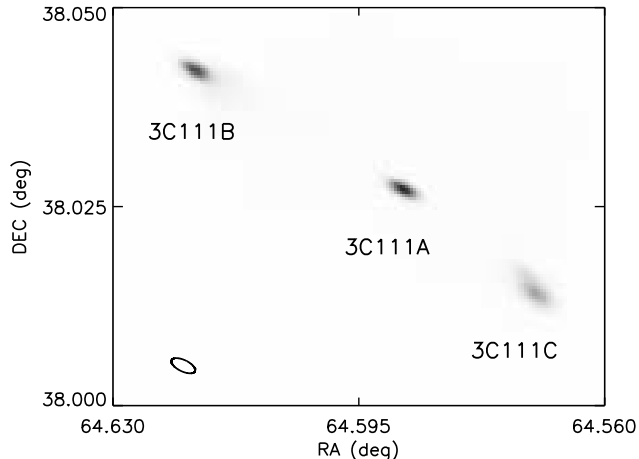


**Figure 1.** The triple-lobed radio galaxy 3C111 shown in 1420 MHz continuum (Murray et al. 2018). Absorption spectra were obtained toward each of its three components, labeled 3C111A, 3C111B, and 3C111C.

TSAS on scales  $\lesssim 1000$  AU (e.g., Johnston et al. 2003; Brogan et al. 2005; Minter et al. 2005; Weisberg et al. 2008; Stanimirović et al. 2010).

Neutral structures at spatial scales of hundreds to thousands of AU can be detected by separately measuring absorption spectra toward each component of a multiple-component radio continuum source (see Figure 1). If the components are separated by a few arcseconds to a few arcminutes, the transverse linear separation of Galactic HI structures between the two lines of sight,  $L$ , is typically  $\lesssim 10^4$  AU. Dickey (1979), Crovisier et al. (1985a), and Greisen & Liszt (1986) have all found significant HI optical depth variations across multiple-component sources with angular separations  $\lesssim 6'$ , suggesting non-uniform HI structure on sub-parsec scales.

Analogous studies have been carried out at optical wavelengths against stars in multiple star systems, which typically probe spatial scales of a few thousand AU (SZ18 and references therein). Several of these observations have suggested that AU-scale structure is especially common in the direction of supernova remnants (Dirks & Meyer 2016; Kameswara Rao et al. 2017) and perhaps stellar bow shocks (Meyer et al. 2015) and the interfaces of warm cloud collisions (Meyer et al. 2012).

Under the assumption that the optical depth variations seen on small angular scales are caused by the presence of discrete HI structures, the measured column density difference divided by the assumed line-of-sight length provides an estimate of the HI number density. Observationally inferred TSAS densities ( $\sim 10^4$ – $10^6$   $\text{cm}^{-3}$ ) and thermal pressures ( $\sim 10^6$ – $10^7$   $\text{K cm}^{-3}$ ) are several orders of magnitude higher than what is com-

mon in either the CNM or the WNM. This has led to several alternative interpretations for the origin of the HI optical depth variations, including the suggestion that the variations could be caused by the overlapping of HI sheets and filaments along the line of sight (Heiles 1997), or the general turbulent cascade over a range of HI structures (Deshpande 2000).

Simulations investigating the formation of TSAS have been rare because of the AU-scale spatial resolution required. Koyama & Inutsuka (2002) performed a two-dimensional numerical hydrodynamic simulation of the propagation of a strong shock into the ISM. They found that regions of a shock-compressed layer leading the shock front fragmented into small, cold cloudlets as a result of thermal instability. These cloudlets had temperatures of  $\sim 20$  K and densities of  $n \sim 2000$   $\text{cm}^{-3}$ , similar to the properties attributed to TSAS. Hennebelle & Audit (2007) numerically modeled a turbulent flow of interstellar atomic gas with spatial resolution of  $2 \times 10^{-3}$  pc, finding that both diffuse and dense structures can form at small scales. The dense structures were produced by collisions between CNM fragments that form within the WNM. These simulations suggest that the formation and survival of TSAS may be driven by shocks. If the small-scale variations in HI optical depth are indeed caused by small dense structures, then we ought to detect these variations preferentially in the direction of shocked regions of the ISM, specifically within a post-shock layer. This may explain TSAS’s association with supernova remnants, stellar bow shocks, or warm cloud collisions as noticed at optical wavelengths (Dirks & Meyer 2016; Kameswara Rao et al. 2017; Meyer et al. 2015, 2012), and with the Local Bubble wall in the Stanimirović et al. (2010) radio HI absorption study against the pulsar B1929+10.

Here, we search for evidence of AU-scale atomic structure by measuring the optical depth variations in the direction of the 9 multiple-component background radio continuum sources included in the 21-SPONGE survey (21-cm Spectral Line Observations of Neutral Gas with the VLA; Murray et al. 2015, 2018) and 3 multiple-component background radio continuum sources included in the Millennium Arecibo Absorption-Line Survey (Heiles & Troland 2003a,b). This nearly doubles the sample size of multiple-component background sources with sensitive HI absorption measurements, and represents the most sensitive study of its kind to date. As discussed by Crovisier et al. (1985a), the HI optical depth variations can be measured in two ways. The first is to measure the change in optical depth for each velocity channel,  $\Delta\tau(v)$ . This approach uses only measured quantities and is relatively simple, but it does not

typically allow us to study the properties of individual structures. The second method of quantifying HI optical depth variation is to fit Gaussian components to the optical depth spectra. Each Gaussian function can be considered to represent a unique structure with a peak optical depth, central velocity, linewidth, spin temperature, and column density. One can then compare the properties of the Gaussian components matched to adjacent lines of sight to determine how these structures change on small scales. This method gives more physically meaningful results than measuring the channel-by-channel variations in optical depth, but it assumes that HI spectral lines are well represented with Gaussian functions, and also depends on the reliability of the Gaussian fitting. We focus here only on measuring the spatial variations of HI optical depth profiles. Future follow-up observations will be necessary to measure temporal variations, which can probe even smaller spatial scales. While Heiles (1997) used “TSAS” for structures on scales of less than a few hundred AU by focusing on pulsar HI spectra and VLBI imaging only, a variety of different observational techniques have expanded the TSAS parameter space in more recent years (see SZ18). Therefore, in this paper we refer as TSAS all neutral structures on spatial scales from a few to thousands of AU.

The 21-SPONGE and Millennium survey data used in this study are presented Section 2. In Sections 3 and 4, we discuss the tiny scale changes in observed HI gas properties using the channel-by-channel method and the method of Gaussian fitting, respectively. We then discuss the implications of the variations seen using both methods in Section 5.

## 2. OBSERVATIONS AND DATA

### 2.1. Observations

The 21-SPONGE survey measured Galactic HI absorption spectra against background radio continuum sources with exceptional optical depth sensitivity ( $\sigma_\tau < 10^{-3}$  at a velocity resolution of  $0.42 \text{ km s}^{-1}$ ) using the Karl G. Jansky Very Large Array (VLA). Matching HI emission spectra were measured at  $\sim 4'$  angular resolution using the Arecibo Observatory. In total, 21-SPONGE observed emission and absorption spectra along 57 unique lines of sight to study the physical properties of neutral hydrogen in the Milky Way (Murray et al. 2015, 2018). The 21-SPONGE background sources included 8 double-lobed galaxies (3C018, 3C041, 3C123, 3C225, 3C245, 3C327.1, 3C409, and 3C410) and one triple-lobed galaxy (3C111; Figure 1). Absorption spectra were measured toward each lobe separately. We measure the optical depth variations across each pair

of components; there are 11 component pairs in total (one pair for each double-lobed source, and three pairs for the triple-lobed source). For each component pair, Table 1 lists the name of each component (Columns 1 and 2), the Galactic coordinates of the source (Columns 3 and 4), the angular separation of the the component pair (Column 5), and the average equivalent width of the HI optical depth toward the two components, defined as  $\int \langle \tau \rangle dv = \int \frac{\tau_1(v) + \tau_2(v)}{2} dv$  (Column 6).

Heiles & Troland (2003a,b) previously obtained high sensitivity emission-absorption measurements with the Arecibo Observatory along 79 lines of sight, including lines of sight toward the double-lobed galaxies 3C33, 3C75, and 3C98. At  $0.42 \text{ km s}^{-1}$  binning, they reach an optical depth sensitivity of  $\sigma_\tau \approx 0.01$ . Table 1 also lists the properties of the component pairs for these lines of sight. While the Millennium survey’s measurements are less sensitive than those of 21-SPONGE, we include these three sources to increase our sample size.

Four of the multiple-component sources are at low Galactic latitude (3C111, 3C123, 3C409, and 3C410), and 8 sources are at  $|b| > 29^\circ$  (3C018, 3C041, 3C225, 3C245, 3C327.1, 3C33, 3C75, and 3C98). The angular separations between components range from  $5''$  to  $4.2'$ . The positions of these multiple-component background sources in Galactic coordinates are shown in Figure 2 against an all-sky map of HI column density from the HI4PI survey (HI4PI Collaboration et al. 2016) with contours of Galactic CO emission from the Planck Collaboration et al. (2014) survey.

### 2.2. Gaussian fits

Both Heiles & Troland (2003a) and Murray et al. (2018) fit Gaussian features to the HI absorption and emission spectra for each line of sight. The reliability of the Gaussian fitting influences our interpretation (see Section 4).

Heiles & Troland (2003a) used a least-squares fit of Gaussian components to the observed absorption and emission spectra to derive the properties of the Gaussian features. Murray et al. (2018) used the Autonomous Gaussian Decomposition algorithm (AGD; Lindner et al. 2015), a derivative spectroscopy program that employs machine learning to estimate the appropriate number of Gaussian features and their properties. The AGD was trained on spectra with the same properties as the Heiles & Troland (2003a) data. Murray et al. (2017) tested the AGD fitting on synthetic spectra (Kim et al. 2014). They found that the completeness—defined as the ratio of the number of AGD-fitted components to the true number of components in the synthetic spectra—was 29% for low Galactic latitudes ( $|b| < 20^\circ$ ), 38% for

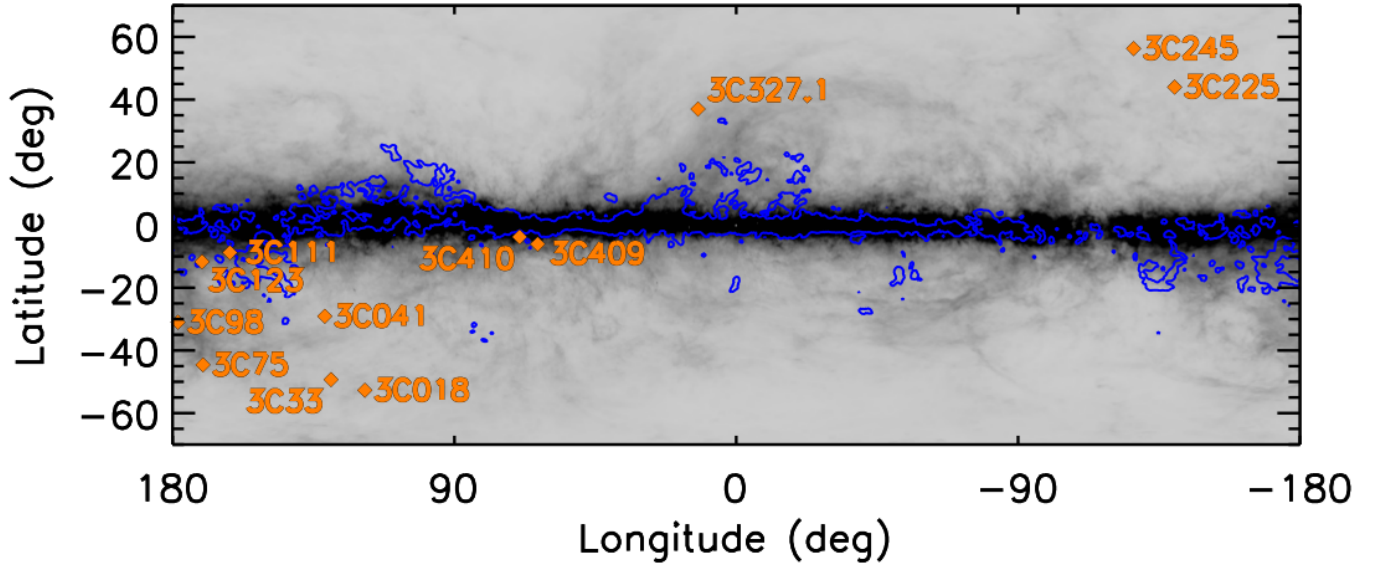


**Figure 2.** An all sky image of the HI column density from the HI4PI survey (HI4PI Collaboration et al. 2016) with the multiple-component sources from the 21-SPONGE and Millennium surveys shown as orange diamonds and labeled in orange text. Blue contours of CO integrated intensity ( $4 \text{ K km s}^{-1}$ ) from the Planck Collaboration et al. (2014) survey of Galactic CO emission are overlaid.

Component 1	Component 2	$\ell$ deg	$b$ deg	$\Delta\theta$	$\langle EW \rangle$ $\text{km s}^{-1}$
3C018A	3C018B	118.6	-52.7	$49''$	$2.37 \pm 0.02$
3C041A	3C041B	131.4	-29.1	$23''$	$0.41 \pm 0.03$
3C111A	3C111B	161.7	-8.8	$2'$	$10.17 \pm 0.03$
3C111A	3C111C	161.7	-8.8	$1.4'$	$10.79 \pm 0.04$
3C111B	3C111C	161.7	-8.8	$3.4'$	$10.76 \pm 0.04$
3C123A	3C123B	170.6	-11.7	$22''$	$8.93 \pm 0.01$
3C225A	3C225B	220.0	44.0	$5''$	$1.57 \pm 0.02$
3C245A	3C245B	233.1	56.3	$5''$	$0.09 \pm 0.03$
3C327.1A	3C327.1B	12.2	37.0	$12''$	$2.24 \pm 0.04$
3C409A	3C409B	63.4	-6.1	$6''$	$8.60 \pm 0.02$
3C410A	3C410B	69.2	-3.8	$6''$	$17.45 \pm 0.04$
3C33-1 <sup>M</sup>	3C33-2 <sup>M</sup>	129.4	-49.3	$4.2'$	$0.45 \pm 0.06$
3C75-1 <sup>M</sup>	3C75-2 <sup>M</sup>	170.3	-44.9	$3.4'$	$2.47 \pm 0.10$
3C98-1 <sup>M</sup>	3C98-2 <sup>M</sup>	179.8	-31.0	$4'$	$2.96 \pm 0.05$

**Table 1.** The multiple-component sources from the 21-SPONGE survey (Murray et al. 2015, 2018) and the Millennium survey (Heiles & Troland 2003a,b). **Col 1–2:** The first and second components of each component pair. Sources from the Millennium survey are denoted with an “M” superscript; all other sources are from the 21-SPONGE survey. **Col 3:** Galactic longitude of the background source. **Col 4:** Galactic latitude of the background source. **Col 5:** The angular separation of the two components. **Col 9:** The average optical depth equivalent width of the two adjacent lines of sight:  $\langle EW \rangle = \int \frac{\tau_1(v) + \tau_2(v)}{2} dv$  (see Section 3 for discussion).

mid latitudes ( $20^\circ < |b| < 50^\circ$ ), and 83% for high latitudes ( $|b| > 50^\circ$ ). The velocity crowding of structures at lower latitudes poses a challenge to the Gaussian fitting.

The number of fitted Gaussian components for the sightlines considered here ranges from 0 in the case of 3C245B (the only sightline in this sample with no fitted optical depth features, since no features reach the signal-to-noise cutoff of 3) to 13 in the case of 3C410A, which is at the lowest Galactic latitude. The Gaussian fitting was used to estimate the central velocity,  $v_0$ , the full-width at half maximum (FWHM),  $b_{\text{FWHM}}$ , and the peak optical depth,  $\tau_0$ , for Gaussian components seen in HI absorption spectra. By using the corresponding HI emission, Heiles & Troland (2003a) and Murray et al. (2018) ran radiative transfer calculations to estimate the spin temperature,  $T_S$ , for each absorption structure. The column density,  $N(\text{HI})$  was then calculated using  $N(\text{HI}) = 1.064 \times C_0 \times \tau_0 \times b_{\text{FWHM}} \times T_S$ , where  $C_0 = 1.823 \times 10^{18} \text{ cm}^{-2}/\text{K km s}^{-1}$ . Some features were fitted with  $T_S < 10 \text{ K}$ . This was deemed physically unreasonable, so the spin temperature and the HI column density are not known for these features. Finally, the total column density along the line of sight and the CNM fraction were estimated.

### 3. ANALYSIS OF SPECTRA

Figure 3 shows the HI optical depth spectra for each pair of components,  $\tau_1(v)$  and  $\tau_2(v)$  (top panel), as well as their difference,  $\Delta\tau(v) \equiv \tau_1(v) - \tau_2(v)$  (bottom panel) with corresponding uncertainties ( $\pm 3\sigma$ ). For 13 out of 14 pairs, we find channels for which  $\Delta\tau(v) > 5\sigma_{\Delta\tau}$ . Such optical depth variation is the trademark signature of TSAS.

Previously, Dickey (1979) found significant changes in HI optical depth in the direction of only 3 out of 9 multiple-component sources, but Crovisier et al. (1985a) and Greisen & Liszt (1986) detected significant variations across all of the multiple-component sources they observed, numbering 7 and 3, respectively. The two strongest detections made by Dickey (1979) had a sensitivity of  $\sigma_{\Delta\tau} \approx 0.005$ , the most sensitive of all their measurements. All non-detections had noise levels of  $\sigma_{\Delta\tau} \gtrsim 0.01$ . Crovisier et al. (1985a) reached noise levels of  $\sigma_{\Delta\tau} \approx 0.005\text{--}0.05$  and Greisen & Liszt (1986) reached noise levels of  $\sigma_{\Delta\tau} \gtrsim 0.05$ . Our results (Figure 3) and the results of these previous HI absorption studies against multiple-component sources suggest that optical depth variations of at least  $\sim 0.05$  are common for cold HI in the Milky Way on angular scales smaller than a few arcminutes. 3C245 is the only multiple-component source in any of the multiple-component studies with a

noise level  $\lesssim 0.01$  that does not show  $> 5\sigma$  variation in HI optical depth.

Some multiple-component sources—like those detected by Dickey (1979) and Greisen & Liszt (1986)—are highly variable ( $\Delta\tau \gg 0.01$ ) over angular scales of  $\lesssim 1'$  and have shown repeated variations in several studies. Out of 12 background sources in this study, we see the most variation in the direction of 3C111, which is one of the sources where Greisen & Liszt 1986 also saw significant changes in the HI optical depth. 3C111 is located behind the Taurus molecular cloud. Since it is triple-lobed, optical depth variations can be measured across three component pairs (AB, AC, and BC). We find optical depth variations as high as 0.38, 0.35, and 0.47 for the three component pairs. We also find large spatial variations of the HI optical depth profiles in the direction of 3C409 ( $\max\{\Delta\tau(v)\} = 0.28$ ) and 3C410 ( $\max\{\Delta\tau(v)\} = 0.52$ ). All three sources show variations at a level of over  $40\sigma$ , and all are located at low Galactic latitudes (Table 1).

We discuss the changes in the integrated HI optical depth spectra across all of our multiple-component background sources in Section 3.1 and then present a channel-by-channel analysis of the HI optical depth variation in Section 3.2.

#### 3.1. Integrated properties

For each source, we calculate the equivalent width of the change in optical depth,

$$\Delta EW = \int \Delta\tau(v) dv. \quad (1)$$

We also calculate a modified version of the equivalent width,

$$\Delta EW_{abs,3\sigma} = \int \left( |\Delta\tau(v)| - 3\sigma_{\Delta\tau} \right) \delta(\Delta\tau \geq 3\sigma_{\Delta\tau}) dv, \quad (2)$$

where

$$\delta(\Delta\tau \geq 3\sigma_{\Delta\tau}) = \begin{cases} 0 & \text{if } |\Delta\tau(v)| < 3\sigma_{\Delta\tau} \\ 1 & \text{if } |\Delta\tau(v)| \geq 3\sigma_{\Delta\tau} \end{cases}$$

for each velocity channel. This modified equivalent width has the advantage of counting both positive and negative changes in HI optical depth, whereas positive and negative values can cancel out using Equation 1. For the 21-SPONGE spectra, Equations 1 and 2 are evaluated over the entire velocity range. For the three Millennium survey sources, they are evaluated from  $-60 \text{ km s}^{-1}$  to  $60 \text{ km s}^{-1}$ , comparable to the 21-SPONGE velocity range.

Both  $|\Delta EW|$  and  $\Delta EW_{abs,3\sigma}$  tend to be higher for sources with higher average equivalent width,  $\langle EW \rangle =$

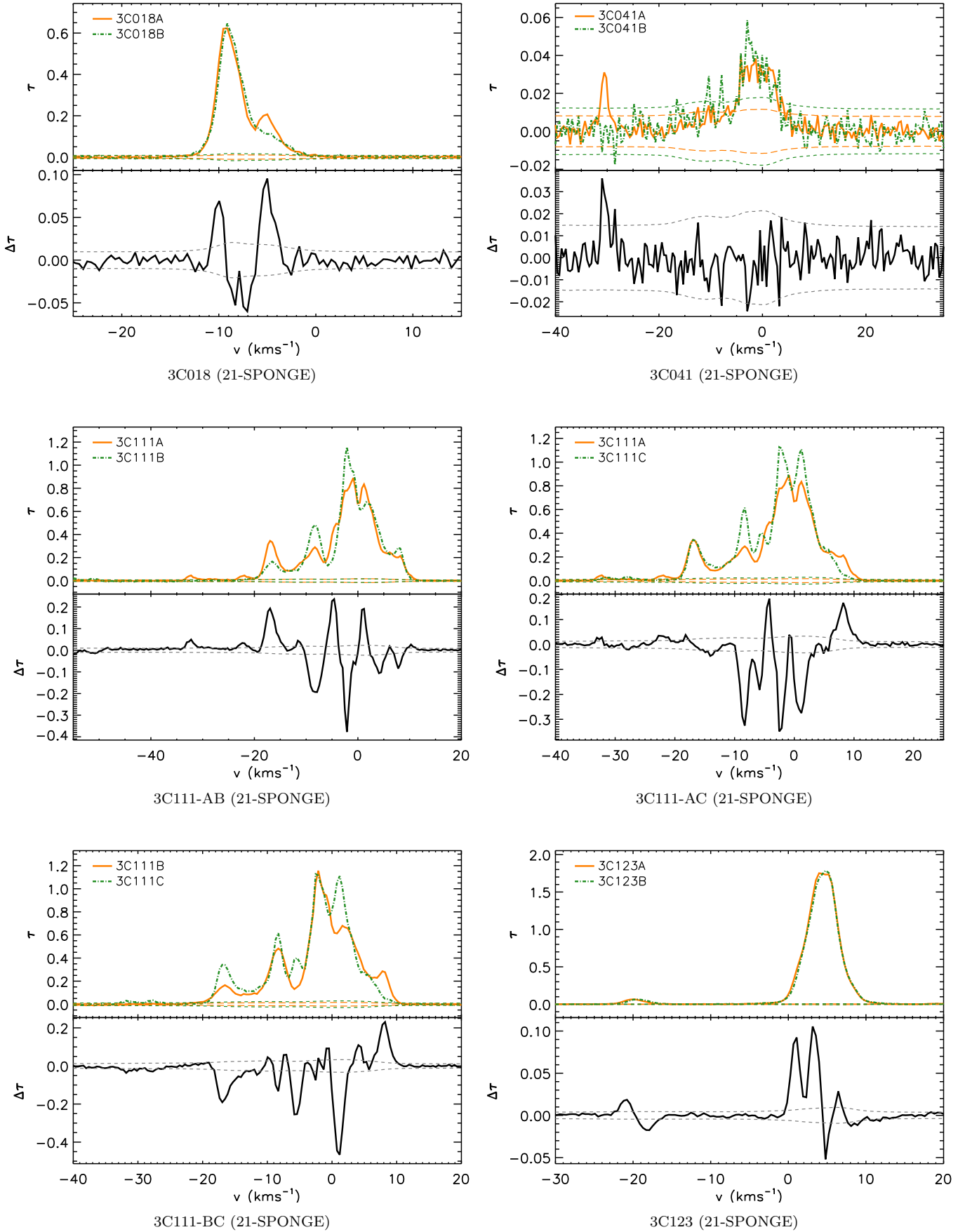


Figure 3.

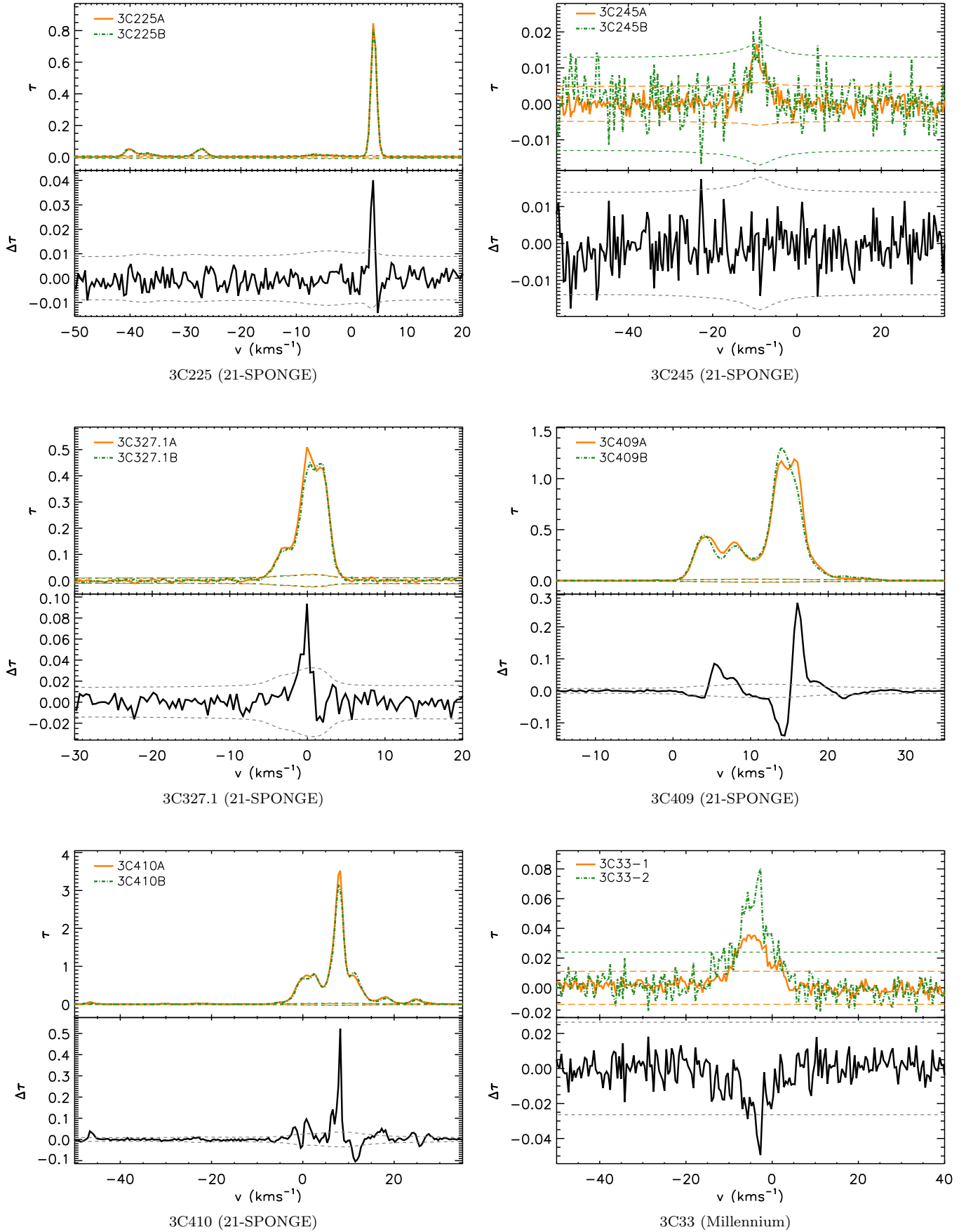
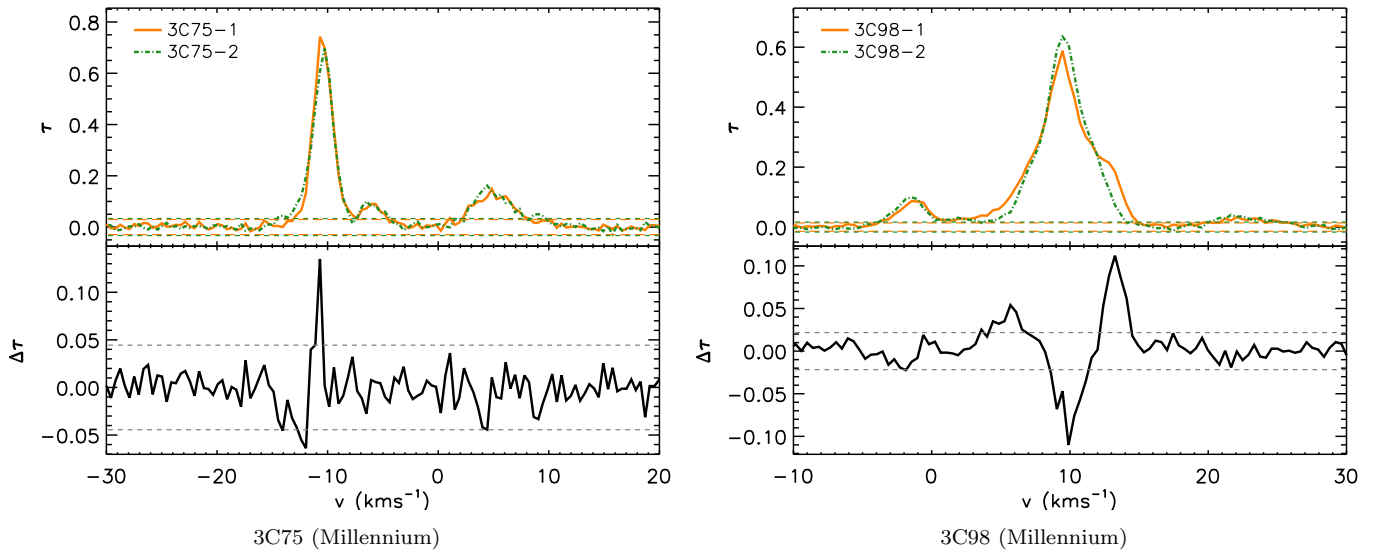
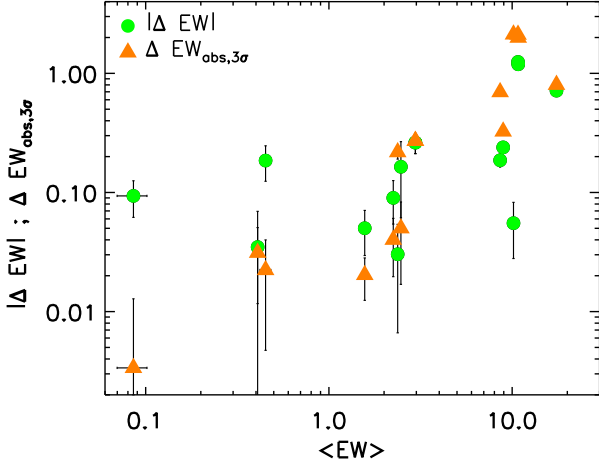


Figure 3.



**Figure 3.** The optical depth,  $\tau(v)$ , for both components (top panels), and the change in optical depth,  $\Delta\tau(v)$ , (bottom panels) for the eleven component pairs from 21-SPONGE and the three component pairs from the Millennium Arcibo Survey multiple-component sources considered in this work.  $3\sigma$  uncertainties are shown as dashed lines for  $\tau(v)$  (both components) and for  $\Delta\tau(v)$ .





**Figure 4.** The absolute value of the change in  $EW$  (green; Equation 1) and  $EW_{obs,3\sigma}$  (orange; Equation 2) versus the average equivalent width,  $\langle EW \rangle = \int \frac{\tau_1(v) + \tau_2(v)}{2} dv$ , for each component pair. This is analogous to Figure 4 of Frail et al. (1994) and Figure 4 of Stanimirović et al. (2010).

$\int \frac{\tau_1(v) + \tau_2(v)}{2} dv$  (Figure 4). This suggests that directions with significant amount of cold HI (often located at low Galactic latitudes) are more likely to host TSAS. This is consistent with what Frail et al. (1994) and Stanimirović et al. (2010) found in their multi-epoch studies of HI absorption against pulsars.

However, the fractional changes in the optical depth equivalent width in our sample,  $|\Delta EW|/\langle EW \rangle$ , are somewhat larger than those found by Stanimirović et al. (2010) at much smaller scales (6 – 50 AU). Here,  $|\Delta EW|/\langle EW \rangle$  ranges from  $< 1\%$  to  $> 100\%$  with a median of 6.6%. The fractional variation of our modified equivalent width,  $\Delta EW_{obs,3\sigma}/\langle EW \rangle$ , ranges from  $\sim 2\%$  to  $\sim 20\%$ , with a median of 7.6%, which is still larger than what was found by Stanimirović et al. (2010),  $\sim 4\%$ . This may suggest that the fractional variation of  $EW$  is larger when probing larger angular/linear separations. While we do not know the distance to the absorbing HI, based on Table 3, most of our multiple-component sources likely probe linear separations of  $\sim 10^3$  to  $\sim 10^5$  AU. This estimate comes from assuming scale height for the CNM of 100 pc (e.g., Baker & Burton 1975; Crovisier 1978) and calculating distance as  $D = 100 \text{ pc} / \sin |b|$ . The sources that show the highest fractional variation are 3C245 (110%) and 3C33 (41%), but the fractional variation of  $\Delta EW_{obs,3\sigma}$  for these sources is typical (4% and 5%, respectively). 3C111, one of our low latitude sources (which is in the direction of the Taurus molecular cloud) shows the highest fractional variation of  $\Delta EW_{obs,3\sigma}$ , about 20% between any two components.

In summary, directions with a significant amount of cold HI show more variation in  $EW$  than directions with a lower cold HI fraction. As most of our sources likely probe linear scales larger than what is commonly probed with pulsars or VLBI imaging, our results may suggest that larger fractional variation in  $EW$  is found on larger spatial scales.

### 3.2. Channel-by-channel properties

A more fine-grained analysis of optical depth variation can be done by considering  $\Delta\tau(v)$  for each velocity channel. In Figure 5, we show the maximum change in HI optical depth,  $|\max\{\Delta\tau(v)\}|$ , versus the average HI optical depth equivalent width,  $\langle EW \rangle$ , for all component pairs. The color in this figure shows the Galactic latitude and the sizes of the points indicate the total HI column density,  $N(\text{HI})_{\text{tot}}$ , from Murray et al. (2018) and Heiles & Troland (2003b). The maximum variations in HI optical depth for these sources show a significant correlation with  $\langle EW \rangle$ , in agreement with Figure 4. This figure is especially striking as it covers a range in maximum optical depth variations from  $\sim 0.03$  to  $\sim 0.5$ , a factor of  $\sim 15$ , demonstrating that our sources are probing diverse interstellar environments. Sources with the highest optical depth variations are those at low Galactic latitudes (3C111, 3C123, 3C409, and 3C410 are all at  $|b| < 12^\circ$ ). They also have the highest HI column densities (Figure 5) and tend to have the highest CNM fractions, defined as the ratio of the CNM column density to the total column density,  $f_{\text{CNM}} = N(\text{HI})_{\text{CNM}}/N(\text{HI})_{\text{tot}}$ . This again indicates that regions at low latitudes with the highest amount of cold HI tend to show the most HI optical depth variation. A similar trend was found by Greisen & Liszt (1986) for the multiple-component sources 3C111 and 3C348.

We note that Murray et al. (2018) and Heiles & Troland (2003b) also estimated the fraction of thermally unstable WNM along each line of sight, although often these estimates have large uncertainties. We do not find a correlation between the magnitude of the optical depth variation and the fraction of thermally unstable WNM.

The maximum change in optical depth as a fraction of the average equivalent width,  $\max\{\Delta\tau(v)\}/\langle EW \rangle$ , is the greatest for sources with lowest optical depth and at the highest Galactic latitudes (Figure 6). The point sizes in Figure 6 indicate the CNM fraction, discussed above. The sources that show the highest fractional variations are 3C245, 3C33, and 3C041, with fractional changes of 0.21, 0.11, and 0.09, respectively. All three sources probe HI environments with a very low peak HI optical depth ( $< 0.1$ ) and relatively low total HI column den-

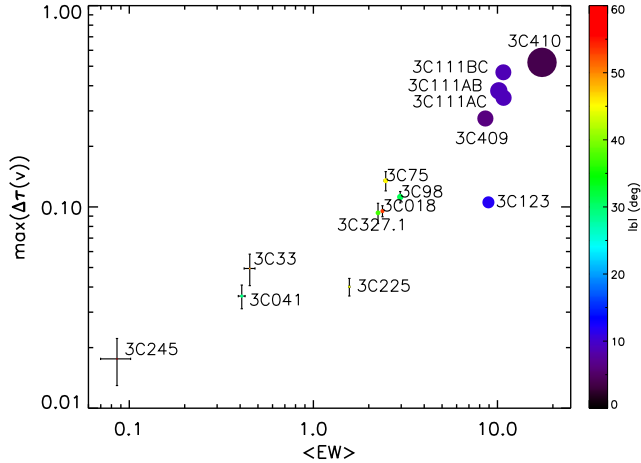


**Figure 5.** The maximum change in HI optical depth versus the average equivalent width for all fourteen component pairs. Points are colored according to Galactic latitude and sized according to total HI column density,  $N(\text{HI})_{\text{tot}}$ .  $N(\text{HI})_{\text{tot}}$  ranges from  $2.1 \times 10^{20} \text{ cm}^{-2}$  to  $4.8 \times 10^{21} \text{ cm}^{-2}$ .

sity ( $\lesssim 5 \times 10^{20} \text{ cm}^{-2}$ ); two of the three sources (3C245 and 3C041) have a very low CNM fraction ( $f_{\text{CNM}} \lesssim 0.1$ ; Murray et al. 2018); and all three have an optical depth feature that appears only in one of two lines-of-sight. In the optical depth spectrum of 3C041, the TSAS feature at  $-30 \text{ km s}^{-1}$  appears only toward the A component and is isolated from the main line in velocity, so clearly stands out in  $\Delta\tau/\tau$ . 3C245, although with a lower signal-to-noise, has a similar TSAS feature at  $-20 \text{ km s}^{-1}$  which appears only in one line of sight. In the case of 3C33, which also has low signal-to-noise, the main line at  $0 \text{ km s}^{-1}$  significantly changes between two components due to appearance of a TSAS feature. For all other background sources,  $\max\{\Delta\tau(v)\}/\langle EW \rangle \sim 3\text{--}5\%$ . The low latitude source 3C123 has the lowest fractional change,  $\sim 1\%$ .

In agreement with Figure 4, then, we see that TSAS is more abundant where the HI optical depth, the HI column density, and the CNM fraction are higher. However, the fraction of the HI optical depth that is occupied by TSAS is the largest and the most prominent where the HI optical depth (and the total HI column density) are the lowest. Barlow (1993), Lundgren et al. (2007), and Hacker et al. (2013) found a similar trend in the temporal variations of narrow quasar absorption lines in external galaxies. While investigating several possible reasons for the variability of absorption lines, including bulk motions of the absorbers and the changing levels of ionization, Lundgren et al. (2007) concluded that the most likely explanation is the change in the covering factor of TSAS (their Figure 2). Essentially, for

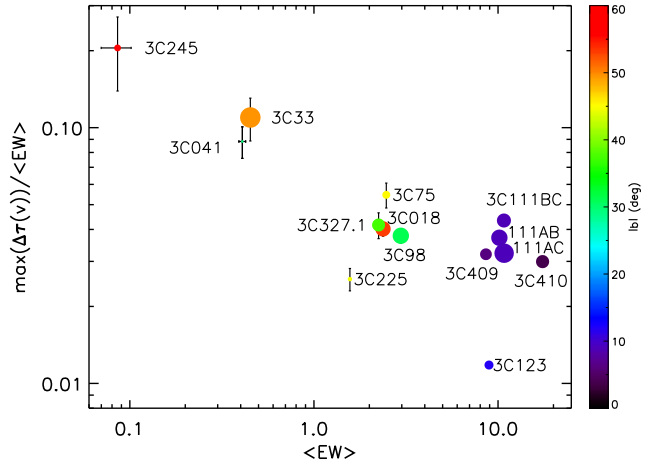


**Figure 6.** The maximum change in optical depth as a fraction of the of the average equivalent width versus the average equivalent width for all fourteen component pairs. Points are colored according to Galactic latitude and sized according to their CNM fractions,  $f_{\text{CNM}} = N(\text{HI})_{\text{CNM}}/N(\text{HI})_{\text{tot}}$ .  $f_{\text{CNM}}$  ranges from 0.0 to 0.67.

the lines of sight with a large  $EW$ , TSAS occupies only a small fraction of the absorption profile and is harder to distinguish than in the directions with a lower optical depth and  $EW$ , where TSAS stands out and is much easier to notice.

#### 4. GAUSSIAN ANALYSIS OF FEATURES

Heiles & Troland (2003a) and Murray et al. (2018) fit Gaussian functions to the HI absorption and emission spectra, deriving the peak optical depth ( $\tau_0$ ), the central velocity ( $v_0$ ), the FWHM ( $b_{\text{FWHM}}$ ), the spin temperature ( $T_S$ ), and the HI column density ( $N(\text{HI})$ ) of the HI structure associated with each feature. Here we investigate the variations in these fitted quantities across the multiple-component sources to isolate the root of the variations seen in global measures like  $EW$ .

We note that Gaussian fitting is not unique, and is especially challenging for lines of sight with multiple HI structures that are close in velocity space (e.g., the low latitude sources; see Figure 3 and discussion in Section 2.2). However, because Gaussian decomposition is useful to investigate important physical characteristics of TSAS—including its thermal and turbulent properties, discussed below—we proceed with the assumption that the Gaussian fits from Heiles & Troland (2003a) and Murray et al. (2018) adequately describe the true properties of the HI structures along the line of sight. The Gaussian fitting also implicitly assumes that the linewidths of absorbing HI structures are larger than the velocity resolution,  $0.42 \text{ km s}^{-1}$ . If linewidths are narrower than the velocity resolution, then the fitted

Gaussian components may span multiple discrete structures.

#### 4.1. Matching Components from Different Lines of Sight

Because the lines of sight to the different lobes of multiple-component galaxies are so close, we expect to see many of the same features in their optical depth spectra (i.e., we expect the same Galactic HI structures to absorb radiation along both lines of sight). For components fitted to adjacent lines of sight to be considered a unique feature (the same absorbing structure), we demand that

$$\delta_{v1,2} \equiv \frac{|v_{0,1} - v_{0,2}|}{b_{\text{FWHM},1}/2.355} \leq 1, \quad (3)$$

where the subscripts 1 and 2 indicate the two separate lines of sight. We also require that  $\delta_{v2,1} \leq 1$ , essentially requiring that the central velocities are within one standard deviation of the linewidths. If multiple features in the adjacent line of sight satisfy these criteria for a given feature, we select the feature that minimizes  $\langle \delta \rangle = (\delta_{v1,2} + \delta_{v2,1})/2$  as the match.

We identify 54 matches in total. We shall henceforth refer to these as the matched features. For 8 of the matched features, we do not have information about  $N(\text{HI})$  or  $T_S$  (these were the features fitted with the unrealistic  $T_S < 10$  K; see Section 2.2).

For 56 features, we do not find a matching feature in the neighboring line of sight (i.e., these features appear along only one line of sight). We shall refer to these as the unmatched features. The unmatched features are particularly interesting candidates for TSAS, since the sizes of the absorbing structures appear to be smaller than the linear separation of the HI between the two lines of sight (i.e.,  $\lesssim 10^5$  AU). Unfortunately, though, for 28 of these features, we do not have  $N(\text{HI})$  or  $T_S$ . While some of these components could be artifacts of Gaussian fitting, for components where there is a large disparity in angular resolution between HI emission and absorption  $T_S$  is impossible to constrain (e.g., Murray et al. 2015).

Table 4 lists the properties of the fitted Gaussian components for all matched and unmatched features from Murray et al. (2018) and Heiles & Troland (2003a). In the following scatter plots, the data corresponding to unmatched features are shown as black triangles. The data corresponding to matched features are shown as circles with colors indicating the value of  $\langle \delta \rangle$  (a lower  $\langle \delta \rangle$  suggests a better match). Likewise, in the stacked histograms, the relative contributions of the unmatched and matched features are shown in green and orange, respectively.

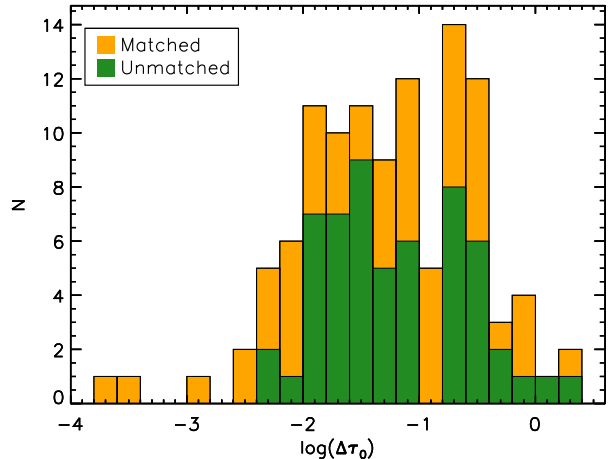


**Figure 7.** The distribution of optical depth variations, in  $\log_{10}$ , for all Gaussian features. For matched features, shown in orange,  $\Delta\tau_0 = |\tau_{0,1} - \tau_{0,2}|$ . For unmatched features, shown in green,  $\Delta\tau_0 = \tau_0$ .

#### 4.2. Variations of Gaussian Components

##### 4.2.1. Peak Optical Depth Variations

The distribution of  $\Delta\tau_0$  (where  $\Delta\tau_0 = |\tau_{0,1} - \tau_{0,2}|$  for matched features and  $\Delta\tau_0 = \tau_0$  for unmatched features) is shown in Figure 7. A majority of the variations are small ( $\Delta\tau < 0.1$ ), but there are a number of features with very large variations, including 8 with  $\Delta\tau > 0.5$ . Table 2 compares the optical depth variations seen in this study to previous multiple-component studies (Crovisier et al. 1985a; Greisen & Liszt 1986). We see a larger average change in the peak optical depth than these previous studies, but the velocity resolution of the absorption spectra used here is  $\sim 0.42$   $\text{km s}^{-1}$ , which is a factor of 2–3 times higher than the velocity resolution of the previous studies. Moreover, these previous studies had non-uniform velocity resolution across different sources, whereas the data in this survey all have the same velocity resolution. If we smooth 21-SPONGE spectra to 2  $\text{km s}^{-1}$  resolution, which is closer to the typical resolutions of Crovisier et al. (1985a) and Greisen & Liszt (1986), we find  $\langle \Delta\tau \rangle \approx 0.10$  (although fewer components are fitted). Similarly, although the average optical depth probed in this study is close to that of previous studies (Table 2), if we restrict our sample to features with optical depths  $> 0.1$ , similar to their sensitivities, we find  $\langle \tau \rangle \approx 0.47$ . We also see a larger spread in optical depth variations than previous studies, which is likely because we are sampling a larger, more diverse sample of interstellar environments, and because we are sensitive to weaker optical depth features.

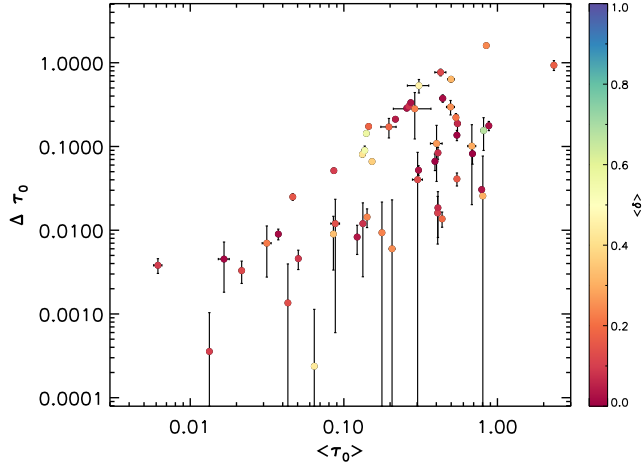


**Figure 8.** The change in peak optical depth,  $\Delta\tau_0$ , versus the average peak optical depth,  $\langle\tau_0\rangle$ , for all matched features. Colors indicate the value of  $\langle\delta\rangle$  (see Section 4.1). Unmatched features are not shown since all fall on a 1-to-1 line.

Figure 8 shows the change in optical depth,  $\Delta\tau_0$ , versus the average optical depth,  $\langle\tau_0\rangle$ , for all matched features. As in Figure 5, we find that the change in the peak optical depth of Gaussian features scales with the optical depth. TSAS is more prominent along lines of sight with higher HI optical depth (i.e., lines of sight with more cold atomic gas).

#### 4.2.2. Central Velocity Variations

The observed optical depth variations seen in Figure 3 do not appear to be a product of changes in the central velocities of HI structures. Figure 9, analogous to Figure 6 of Lundgren et al. (2007), shows the magnitude of the change in peak optical depth,  $\Delta\tau_0$ , versus the central velocity,  $v_0$ , for each matched feature. It indicates that changes in  $v_0$  tend to be small, while changes in  $\tau_0$  can be dramatic. This is the same conclusion drawn by Greisen & Liszt (1986). Table 2 shows that the small changes we see in central velocities of fitted components are similar to those seen in previous multiple-component absorption studies. Moreover, if we downgrade the velocity resolution of the absorption spectra to 1–2  $\text{km s}^{-1}$  and match components, we find that the changes in central velocity of matched components still tend to be  $< 0.4 \text{ km s}^{-1}$ . Neither the change in peak optical depth nor the change in optical depth equivalent width (Section 4.2.4, below) are correlated with the change in central velocity.

#### 4.2.3. Velocity Width Variations

While changes in the central velocities of matched features tend to be small, changes in their linewidths can be considerable. Figure 10 shows that both the change in peak optical depth ( $\Delta\tau_0$ ) and the change in the velocity

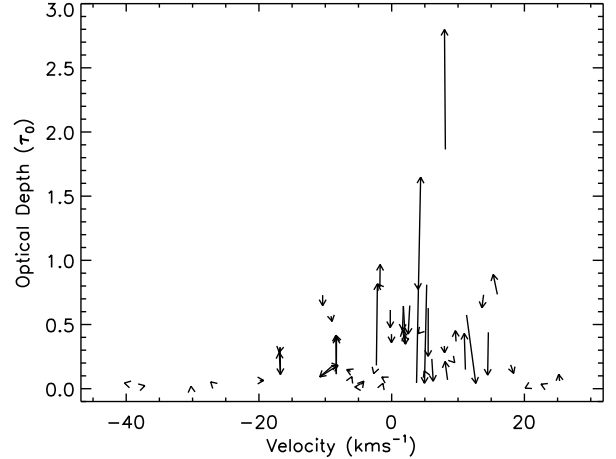


**Figure 9.** Analogous to Figure 6 of Lundgren et al. (2007), the magnitude of the change in peak optical depth versus the central velocity for each matched feature. The direction of the arrows is arbitrary, pointing from Component 1 to Component 2, as listed in Table 1.

width ( $\Delta b_{\text{FWHM}}$ ) can be large for a given feature—both contribute to the observed optical depth variation. This helps explain the variation of the optical depth equivalent width, since both  $\tau_0$  and  $b_{\text{FWHM}}$  contribute to the equivalent width (Section 3.1 and Section 4.2.4, below).

While there are features with drastic linewidth changes (five features with  $\Delta b_{\text{FWHM}} \sim 4\text{--}7 \text{ km s}^{-1}$  and one outlier with  $\Delta b_{\text{FWHM}} \sim 15 \text{ km s}^{-1}$ ), in most cases we find a smaller but clearly noticeable linewidth change of 1–2  $\text{km s}^{-1}$ . This can be seen in Figure 11 which compares the two FWHMs of each matched feature,  $b_{\text{FWHM},1}$  and  $b_{\text{FWHM},2}$ . The dashed line represents a 1-to-1 match. We see that extreme outliers tend to be more poorly matched, even though they satisfy our matching criterion (see Section 4.1). A majority of components lie just below (or slightly above) the 1-to-1 line, offset by  $\lesssim 1\text{--}2 \text{ km s}^{-1}$ . As the velocity linewidth comes from both thermal motions and turbulent motions, we investigate both further (Sections 4.2.5 and 4.2.6, respectively).

#### 4.2.4. Equivalent Width Variations

The equivalent width of a given Gaussian feature is

$$EW_0 = 1.064 \times \tau_0 \times b_{\text{FWHM}}. \quad (4)$$

In Figure 12, we show the distribution of the change in equivalent width ( $\Delta EW_0 = |EW_{0,1} - EW_{0,2}|$  for matched features and  $\Delta EW_0 = EW_0$  for unmatched features). This level of variation is consistent with the equivalent width variation seen in previous multiple-component absorption experiments (Table 2), although

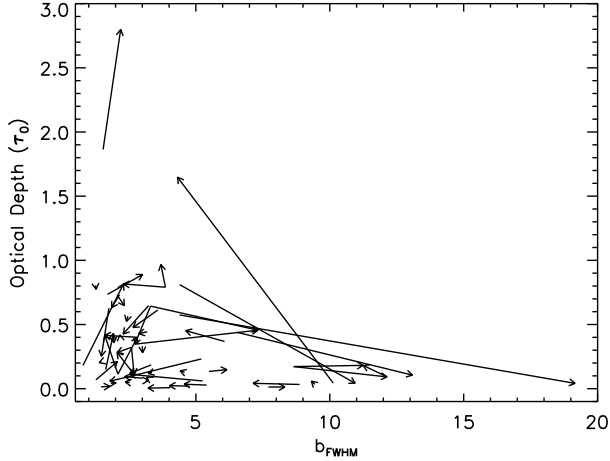


**Figure 10.** Analogous to Figure 5 of Lundgren et al. (2007), the magnitude of the change in peak optical depth versus the linewidth for each matched feature. The direction of the arrows is arbitrary, pointing from Component 1 to Component 2, as listed in Table 1.

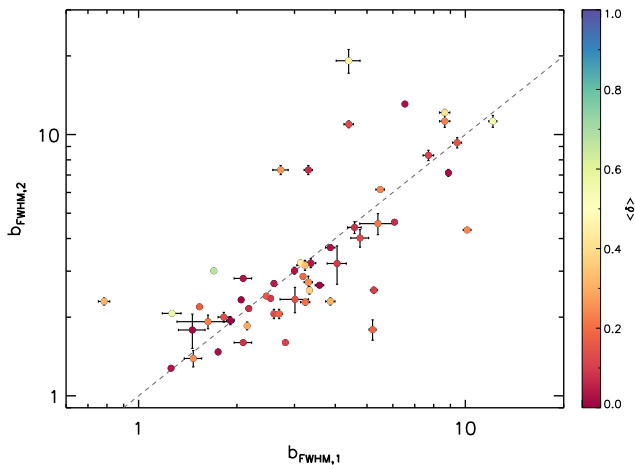


**Figure 11.** A comparison of the FWHMs of matched features,  $b_{\text{FWHM},2}$  versus  $b_{\text{FWHM},1}$ . Colors indicate the average value of  $\delta$  of the matched features (see Section 4.1).

we see a larger spread in the variations. This is particularly noteworthy because the optical depth equivalent width does not depend on the velocity resolution, unlike, e.g., the peak optical depth. Figure 13 indicates that greater equivalent width variations tend to be associated with higher average equivalent widths,  $\langle EW_0 \rangle$ , for matched features<sup>1</sup>. This is consistent with what we see in Figures 4 and 5, and agrees with the trend

<sup>1</sup> We do not plot here unmatched features as they all lie on the 1-to-1 line

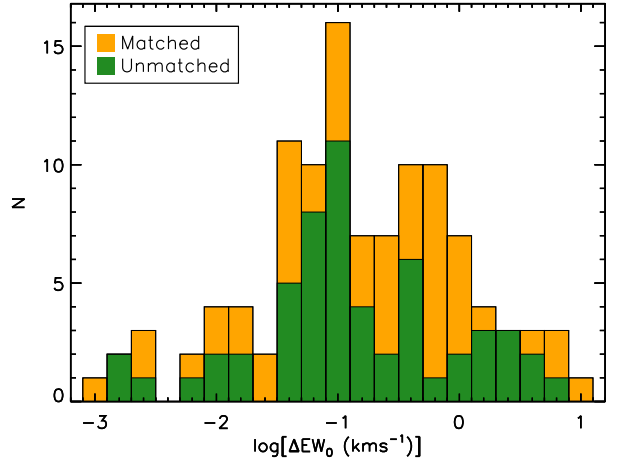


**Figure 12.** The distribution of optical depth equivalent width variations (Equation 4), in  $\log_{10}$ , for all Gaussian features. For matched features, shown in orange,  $\Delta EW_0 = |EW_{0,1} - EW_{0,2}|$ . For unmatched features, shown in green,  $\Delta EW_0 = EW_0$ .

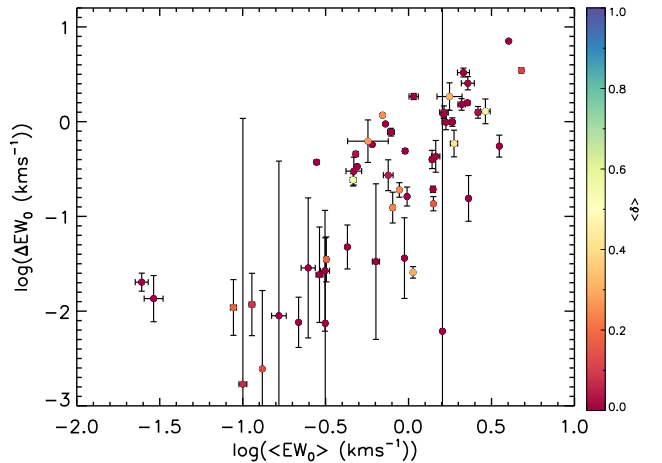


**Figure 13.** The change in HI optical depth equivalent width,  $\Delta EW_0$ , as a function of the average optical depth equivalent width,  $\langle EW_0 \rangle$ , for matched features. Points are colored based on the value of  $\delta$  (see Section 4.1). Unmatched features are not shown since all lie on the 1-to-1 line.

seen in narrow quasar absorption lines by Hacker et al. (2013). The HI optical depth variation is strongest toward lines of sight sampling more cold atomic gas (Section 3.2). As discussed above, this variation is likely a product of changes in both the peak optical depths and the linewidths.

#### 4.2.5. Spin Temperature Properties

The spin temperature, which is a good estimate of the kinetic temperature for the CNM, was determined for

most features in the 21-SPONGE survey (Murray et al. 2018) and the Millennium Arecibo 21-cm survey (Heiles & Troland 2003a). However, as described in detail in Murray et al. (2018), the 21-SPONGE survey estimated  $T_S$  using both the VLA HI absorption spectra as well as HI emission spectra from the Arecibo Observatory. The emission data therefore have a resolution of  $\sim 4'$ , which is larger than the typical separation between multiple-component pairs in this study, meaning that our  $T_S$  estimates for the different components of each source were not from independent HI emission data. Thus, we unfortunately do not have a clear probe of spin temperature variations across multiple components. Higher angular resolution HI emission observations are needed to investigate the question of whether  $T_S$  changes significantly between multiple components.

If we neglect turbulent fluctuations and assume only thermal motions, though, we can place some constraints on how large temperature fluctuations are needed to explain the observed change in linewidth (Section 4.2.3)<sup>2</sup>. For example, for a Gaussian feature that is  $3 \text{ km s}^{-1}$  wide to change linewidth by  $1\text{--}2 \text{ km s}^{-1}$ , an increase in kinetic temperature of  $\sim 130\text{--}260 \text{ K}$  would be required. For a Gaussian feature that is  $8 \text{ km s}^{-1}$  wide to change linewidth by  $1\text{--}2 \text{ km s}^{-1}$ , we would need an increase in kinetic temperature of  $\sim 350\text{--}700 \text{ K}$ . For a typical CNM temperature of  $50 \text{ K}$ , this means that a significant temperature increase would be needed to explain the observed changes in linewidth. We cannot dismiss even this simplified scenario, though, as Hennebelle & Audit (2007) showed that small, dense structures suggestive of TSAS form with a steep temperature gradient. For example, a structure  $\lesssim 10^5 \text{ AU}$  in size with a central temperature of  $\sim 200 \text{ K}$  may rise to  $\sim 4000 \text{ K}$  in the outskirts of the structure. The 3D magnetohydrodynamic (MHD) simulation of Inoue & Inutsuka (2012), in which HI accretion flows lead to the formation of a highly inhomogeneous molecular cloud comprising dense cold clumps embedded in a warmer diffuse medium, found similarly strong temperature gradients on scales  $< 1 \text{ pc}$  (their Figure 4).

We can also investigate whether Gaussian components with optical depth variations show unusual physical properties. For example, in a pulsar study of TSAS Stanimirović et al. (2010) found that the spin temperature in the direction of B1929+10—the only source in their sample that showed repeated variations of HI absorption spectra over time—was significantly higher ( $150\text{--}200 \text{ K}$ ) than what is typically found for the CNM

<sup>2</sup> We discuss the contribution of turbulence to the linewidths in Section 4.2.6

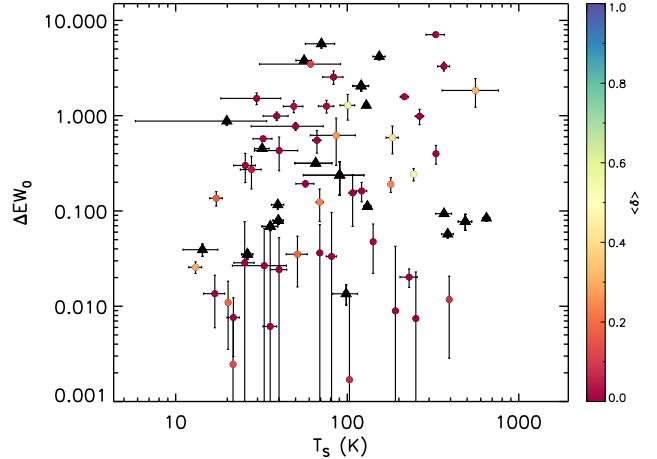


**Figure 14.** The change in optical depth equivalent width (Equation 4) versus spin temperature,  $T_S$ . For matched features,  $\Delta EW_0 = |EW_{0,1} - EW_{0,2}|$  and the x-axis shows  $\langle T_S \rangle$ . Matched features are shown as circles with colors indicating the value of  $\langle \delta \rangle$  (see Section 4.1). For unmatched features,  $\Delta EW_0 = EW_0$  and the x-axis is  $T_S$ . Unmatched features are shown as black triangles.

(e.g.,  $20\text{--}70 \text{ K}$ ). The same line of sight has also a very low CNM fraction and is believed to be sampling the Local Bubble wall. In Figure 14 we show the difference in optical depth equivalent width (Equation 4) as a function of spin temperature for both matched and unmatched features. For matched features, the x-axis shows the average spin temperature of the matched features,  $\langle T_S \rangle$ . For unmatched features, the x-axis is  $T_S$ . While we do not see a correlation, it is clear from this plot that most of the variation is associated with the CNM ( $T_S \lesssim 260 \text{ K}$ ; Wolfire et al. 2003).

#### 4.2.6. Turbulent properties

Turbulence has been suggested as a possible driver of TSAS formation, since compressible turbulence in the ISM produces density fluctuations and may even be sufficient to confine overpressured structures (SZ18). Here, we are able to measure the turbulent velocity of the Gaussian features,  $\sigma_{v_0,t}$ , which allows us to compare the thermal pressure and turbulent pressure of TSAS structures and to test the influence of turbulence on the observed optical depth variations. The 1D turbulent velocity for each component is given by

$$\begin{aligned} \sigma_{v_0,t}^2 &= \sigma_{v_0}^2 - k_B T_S / m_H \\ &= \left( \frac{b_{\text{FWHM}}}{2.355} \right)^2 - k_B T_S / m_H, \end{aligned} \quad (5)$$

where  $m_H$  is the mass of the hydrogen atom, and the spin temperature,  $T_S$ , is a proxy for the kinetic temperature,

$T_{kin}$ , which is reliable for the CNM (this is equivalent to Equation 16 of Heiles & Troland 2003b). Because  $\sigma_{v_0,t}$  depends on the temperature, we cannot reliably measure the change in turbulent velocity between matched features (see Section 4.2.5). Nevertheless, we can estimate a characteristic turbulent velocity,  $\langle\sigma_{v_0,t}\rangle$ , the average 1D turbulent velocity between the two matched components, evaluated with Equation 5 using  $b_{FWHM,1}$  and  $T_{S,1}$  for the first component and  $b_{FWHM,2}$  and  $T_{S,2}$  for the second component.

Figure 15 shows the change in optical depth equivalent width (Equation 4) versus the 1D turbulent velocity for each feature. There is a marginally increasing trend ( $\log \Delta EW_0 \propto (0.98 \pm 0.28) \log \sigma_{v_0,t}$ ), with the largest variations tending to be associated with the highest turbulent velocities. We see that the 1D turbulent velocities range from  $\sim 0.3$  to  $\sim 4.7$   $\text{km s}^{-1}$ , and are therefore a non-negligible contribution to the velocity linewidths. Brogan et al. (2005) argued that spin temperature variation is not the primary cause of TSAS after they found strong agreement between the linewidths of HI features observed with both the Very Long Baseline Array (VLBA) and the Arecibo Observatory (Heiles & Troland 2003b). But this assumes that thermal broadening dominates turbulent broadening, which these results suggest is not a safe assumption. Furthermore, these turbulent velocities are similar to or larger than the typical sound speed in the CNM. This suggests the need of a driver to sustain supersonic turbulence.

We also compare the turbulent pressure,  $P_{turb} = \rho \sigma_{v_0,t}^2$ , to the thermal pressure,  $P_{th} = nk_B T$ , using the ratio

$$r = \frac{k_B T_S}{m_H \sigma_{v_0,t}^2}, \quad (6)$$

where  $T_S$  is again a proxy for the kinetic temperature. For matched features, we use the average 1D turbulent velocity,  $\langle\sigma_{v_0,t}\rangle$ , and the average spin temperature,  $\langle T_S \rangle$ , when evaluating Equation 6. The uncertainties on the spin temperatures and turbulent velocities for matched features due to variations in the spin temperature (Section 4.2.5) lead to a typical uncertainty of  $\sim 20$ – $30\%$ . The distribution of  $r$  is shown in Figure 16. For a majority of features, turbulent pressure is dominant (i.e.,  $r < 1$ ).

Based on McKee & Zweibel (1992), SZ18 estimate that the turbulent velocity must exceed the rms velocity by a factor of at least 10 to confine a structure that is overpressured by a factor of 100. In Figure 17, we show the 1D rms velocity versus the 1D turbulent velocity. We show lines indicating a 1-to-1 ratio (dotted), and a 1-to-10 ratio (dashed). All points lie above the dashed line, indicating that the turbulent velocity is likely too

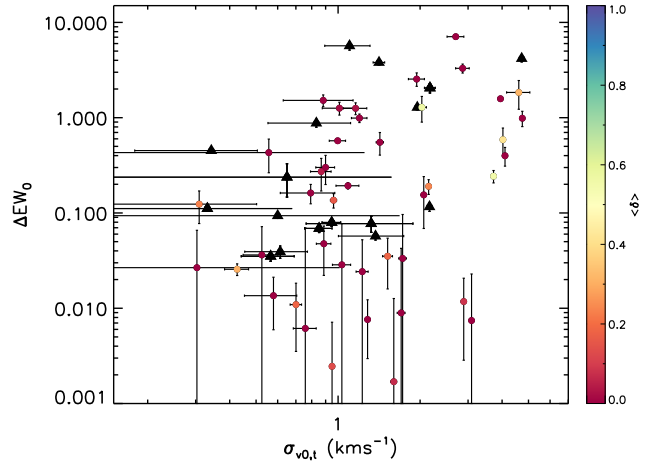


**Figure 15.** The change in optical depth equivalent width versus the 1D turbulent velocity for all Gaussian features with known  $T_S$ . For matched features,  $\Delta EW_0 = |EW_{0,1} - EW_{0,2}|$  and the x-axis shows the average 1D turbulent velocity of the two features. Matched features are shown as circles with colors indicating the value of  $\langle\delta\rangle$  (see Section 4.1). For unmatched features,  $\Delta EW_0 = EW_0$  and the x-axis is the 1D turbulent velocity of the single feature. Unmatched features are shown as black triangles.

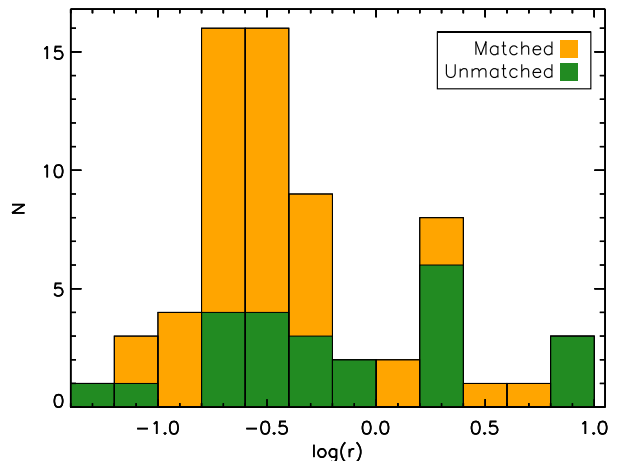


**Figure 16.** The distribution of  $r$  (Equation 6), in  $\log_{10}$ , for all Gaussian features. The contribution from the unmatched features is shown in green, while the contribution from the matched features is shown in orange.

small to lead to pressure confinement of the observed TSAS features, suggesting that our TSAS features are expanding or not highly overpressured.

#### 4.2.7. Column Density Variations

The column density of each feature calculated by Murray et al. (2018) and Heiles & Troland (2003a) is listed in Table 4. Since the column density depends on the spin

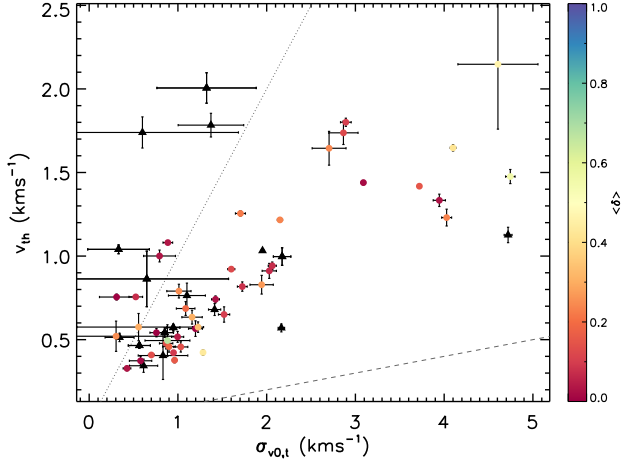


**Figure 17.** The estimated 1D rms velocity,  $\sqrt{k_B T_S / m_H}$ , versus the 1D turbulent velocity (Equation 5). Matched features are shown as circles whose colors indicate the value of  $\langle \delta \rangle$  (see Section 4.1). Unmatched features are shown as black triangles. The dotted line shows the 1-to-1 relationship. The dashed line shows the 1-to-10 relationship that SZ18 estimate would be necessary for turbulent confinement.

temperature, though, the column densities for the two components of each set of component pairs are not independently measured (see beginning of Section 4.2.5). Nevertheless, we use these column density estimates as reasonable approximations because doing so allows us to investigate the column density and density of TSAS.

In Figure 18, we show the distribution of the change in HI column density ( $\Delta N(\text{HI}) = |N(\text{HI})_1 - N(\text{HI})_2|$  for matched features and  $\Delta N(\text{HI}) = N(\text{HI})$  for unmatched features). The median change in column density is  $\Delta N(\text{HI}) = 3.5 \times 10^{19} \text{ cm}^{-2}$ . This HI column density variation is consistent with previous TSAS studies, which have primarily found  $\Delta N(\text{HI})$  between  $10^{19} \text{ cm}^{-2}$  and  $10^{21} \text{ cm}^{-2}$  (see Table 1 of SZ18 and references therein).

A cloud with a sufficiently high column density,  $N_{\text{min},c}$ , may radiatively cool fast enough to prevent expansion, meaning that it can reach thermal equilibrium while being overpressured. SZ18 estimated the critical column density to be  $N_{\text{min},c} = 1.2 \times 10^{15} T^{3/2} e^{92/T} \text{ cm}^{-2}$  by demanding that the cooling time ( $3kT/2n\Lambda$ , where  $\Lambda$  is the radiative loss function) be less than the dynamical time ( $R/\sqrt{kT/m}$ , where  $R$  is the size of the cloud). Taking  $\Delta N(\text{HI})$  to be the TSAS column density and  $T_S$  to be a proxy for the kinetic temperature, we find that 59 of the 79 features with known column densities have column densities exceeding  $N_{\text{min},c}$ , i.e., a majority of the structures could presumably be overpressured but in thermal equilibrium with the ambient ISM.

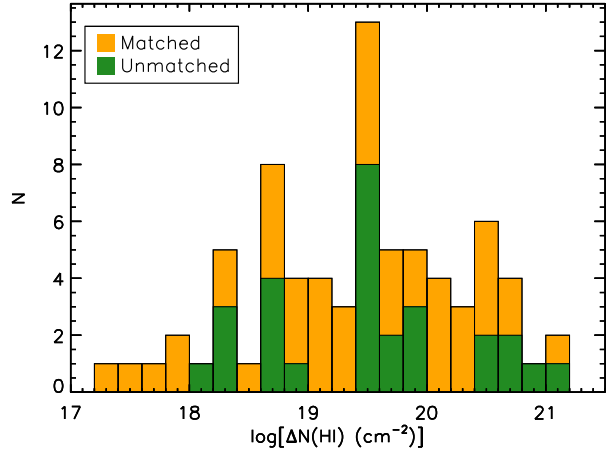


**Figure 18.** The distribution of column density variations, in  $\log_{10}$ , for all Gaussian features. For matched features, shown in orange,  $\Delta N(\text{HI}) = |N(\text{HI})_1 - N(\text{HI})_2|$ . For unmatched features, shown in green,  $\Delta N(\text{HI}) = N(\text{HI})$ .

#### 4.2.8. Estimating density

Under a simple geometric assumption, the change in HI density between adjacent lines of sight is  $\Delta N(\text{HI})/L$ , where  $L$  is the linear separation of HI structures along the line of sight. The linear separation is unknown for most features in our sample because we do not know the distance,  $D$ , to the absorbing HI structures ( $L = D\Delta\theta$ , with  $\Delta\theta$  listed in Table 1). Unfortunately, kinematic distances are unreliable or have extremely large uncertainties ( $\gtrsim 100\%$ ) for most features in this study (e.g., Wenger et al. 2018). Another way of getting a rough distance estimate is by assuming a scale height for the CNM of 100 pc (e.g., Baker & Burton 1975; Crovisier 1978) and taking  $D = 100 \text{ pc} / \sin |b|$ . For the range of angular separations probed here, this yields typical linear separations of  $\sim 10^3$  to  $\sim 10^5$  AU.

Three of our sources are in the direction of structures with well-known distances. We estimate TSAS densities only for these sources. 3C111 and 3C123 are in the direction of the Taurus molecular cloud (Figure 19) and 3C225 is in the direction of the well-studied local Leo cold cloud, first identified by Verschuur (1969). For features whose radial velocities indicate that they are associated with these known clouds ( $\sim -4$ – $10 \text{ km s}^{-1}$  for Taurus and  $4 \text{ km s}^{-1}$  for the Leo cloud; Ungerechts & Thaddeus 1987; Verschuur 1969), we have fairly tight constraints on distance (Taurus from Yan et al. 2019 and the Leo cloud from Peek et al. 2011), so we can estimate the linear separation,  $L$ , and the density,  $\Delta n \approx \Delta N(\text{HI})/L$ , of the TSAS. Table 3 lists the estimated HI densities for these features. Previous studies have found TSAS densities between a few thousand  $\text{cm}^{-3}$



(e.g., Dhawan et al. 2000; Goss et al. 2008) and  $\gtrsim 10^6$   $\text{cm}^{-3}$  (e.g., Moore & Marscher 1995). The results listed in Table 3 are on the lower end of this range, but still exceed typical CNM densities by roughly an order of magnitude ( $n_{\text{CNM}} \lesssim 100 \text{ cm}^{-3}$ ; Wolfire et al. 2003).

#### 4.3. Individual Sources

Several of the multiple-component sources in this study have previously been studied for signs of TSAS (SZ18 and references therein). Some are also associated with known Galactic structures. Here, we compare our observations of these sources to previous studies.

##### 4.3.1. 3C111

3C111, the only triple-lobed background source in our sample, has been observed extensively in absorption studies. It is in the direction of the Taurus molecular cloud (Figure 19).

Dickey & Terzian (1978) measured HI absorption across the B and C components of 3C111, noting significant variation ( $\Delta\tau = 0.32$ ) at  $v = 8.3 \text{ km s}^{-1}$ . Greisen & Liszt (1986) also detected a feature at  $\sim 8 \text{ km s}^{-1}$  present in the B component but absent in both the A and C components. With 21-SPONGE, we see a strong absorption feature at  $\sim 8 \text{ km s}^{-1}$  toward the B component ( $\tau = 0.212$ ) that is greatly diminished toward the (central) A component ( $\tau = 0.069$ ), and vanishes at the C component. Unfortunately, we do not know  $T_S$  or  $N(\text{HI})$  for these features and are therefore unable to estimate the corresponding change in density.

Greisen & Liszt (1986) detected significant spatial variation in an optical depth feature at  $-2 \text{ km s}^{-1}$  that appeared toward all three lobes, but increased to the east. We also see strong absorption toward all three lobes at  $v \sim -2 \text{ km s}^{-1}$  with an eastward increase in optical depth, although the lowest optical depth is observed toward the central A component. Table 3 suggests a density of a few hundred  $\text{cm}^{-3}$  for this TSAS feature, presumably associated with the Taurus molecular cloud complex.

Goss et al. (2008) compared the HI absorption from the A and B components of 3C111, identifying strong variations ( $\Delta\tau \sim 0.3$ ) at  $v \approx -19 \text{ km s}^{-1}$  and  $v \approx -11 \text{ km s}^{-1}$ . While we do not find components at  $-19 \text{ km s}^{-1}$  and  $-11 \text{ km s}^{-1}$ , we do identify variable features at  $-16.8$  and  $-8.3 \text{ km s}^{-1}$  that bear a striking resemblance to their features. If, as we suspect, their features are the same as ours, offset by a velocity of  $\sim 2 \text{ km s}^{-1}$ , then we confirm this variation ( $\Delta\tau_0 \approx 0.2$  for the  $-16.8 \text{ km s}^{-1}$  feature and  $\Delta\tau_0 \approx 0.3$  for the  $-8.3 \text{ km s}^{-1}$  feature).

Marscher et al. (1993) were the first to suggest TSAS in the direction of 3C111 on the basis of molecular ab-

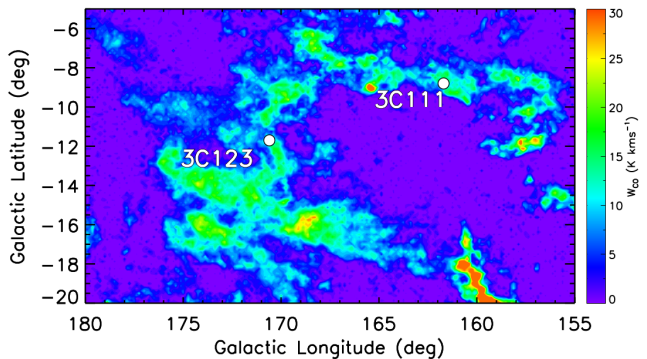


**Figure 19.** Integrated intensity of  $^{12}\text{CO}(1-0)$ ,  $W_{\text{CO}}$ , measured by Dame et al. (2001), in the direction of the Taurus molecular cloud. The positions of two of our background sources, 3C111 and 3C123, are coincident with the molecular cloud.

sorption variations. They detected significant changes in the  $\text{H}_2\text{CO}$  optical depth toward 3C111 over a period of 2.05 yr, suggesting molecular structures with  $n \sim 10^6 \text{ cm}^{-3}$  on scales of  $\lesssim 10 \text{ AU}$ . These results were later supported by Moore & Marscher (1995), who extended the observational time span to 3.4 yr. Moore & Marscher (1995) also detected significant spatial variations in the HI,  $\text{H}_2\text{CO}$ , and OH absorption across 3C111. However,  $\text{H}_2\text{CO}$  absorption variation may be strongly dependent on the gas dynamics, chemistry, or radiation field, rather than the density and column density (Thoraval et al. 1996). This would make it a poor tracer of TSAS compared to dust absorption or HI absorption, which do not suggest TSAS densities as extreme as  $10^6 \text{ cm}^{-3}$ .

Here, we see significant HI optical depth variations across 3C111, with  $\Delta EW_{\text{abs},3\sigma} \approx 20\%$  between any two components—the HI optical depth in the direction of 3C111 is highly variable, and some features appear to undergo large changes in density over spatial scales  $\lesssim 0.1 \text{ pc}$  (Table 3). These changes in density are smaller than those suggested by the  $\text{H}_2\text{CO}$  absorption studies of Marscher et al. (1993) and Moore & Marscher (1995), although we are probing spatial scales several orders of magnitude larger.

The HI absorption features in the direction of 3C111 span a velocity range of over  $30 \text{ km s}^{-1}$ . In Section 4.2.8, we estimate the densities of HI structures whose radial velocities suggest that they are part of the Taurus molecular cloud complex, assuming that components with radial velocities outside this range are well-separated along the line of sight. But it is possible that many or all of the strong HI absorption features are associated with Taurus—the large spread in velocity could be due to the contribution of multiple flows within the molecular cloud complex, driven by, e.g., Herbig-Haro outflows (al-

**Table 2.** Summary of the properties of the Gaussian features. Data from this work are separated into two columns—one for matched features, and another for unmatched features. This is analogous to Table 5 of Greisen & Liszt (1986). The uncertainties on all averaged quantities from this work are all very small. In this table, the standard deviations are shown.

Parameter	This Work	This Work	Greisen & Liszt (1986)	Crovisier et al. (1985)
	Matched	Unmatched		$L < 1$ pc / $L > 1$ pc
$\langle \tau_0 \rangle$	$0.348 \pm 0.369$	$0.174 \pm 0.299$	$0.30 \pm 0.18$	$0.41 \pm 0.21/0.42 \pm 0.28$
$\Delta \tau_0$	$0.167 \pm 0.280$		$0.05 \pm 0.04$	$0.08 \pm 0.08/0.06 \pm 0.06$
$\frac{\Delta \tau_0}{\langle \tau_0 \rangle}$	$0.463 \pm 0.500$		$0.19 \pm 0.20$	$0.27 \pm 0.30/0.18 \pm 0.18$
$\Delta v_0$	$0.31 \pm 0.47$		$0.21 \pm 0.20$	$0.52 \pm 0.34/1.60 \pm 1.47$
$\frac{\Delta v_0}{\langle b_{\text{FWHM}} \rangle}$	$0.07 \pm 0.06$		$0.06 \pm 0.05$	$0.09 \pm 0.08/0.14 \pm 0.11$
$\langle b_{\text{FWHM}} \rangle$	$4.10 \pm 2.83$	$2.57 \pm 1.88$	$2.35 \pm 1.81$	$7.47 \pm 3.81/11.59 \pm 3.93$
$\Delta b_{\text{FWHM}}$	$1.46 \pm 2.46$		$0.49 \pm 0.57$	$0.89 \pm 0.57/2.19 \pm 1.24$
$\frac{\Delta b_{\text{FWHM}}}{\langle b_{\text{FWHM}} \rangle}$	$0.30 \pm 0.30$		$0.31 \pm 0.24$	$0.33 \pm 0.24/0.54 \pm 0.38$
$\langle EW_0 \rangle$	$1.17 \pm 1.05$	$0.58 \pm 1.13$	$1.03 \pm 0.80$	$3.35 \pm 2.57/4.48 \pm 2.76$
$\Delta EW_0$	$0.74 \pm 1.19$		$0.15 \pm 0.15$	$0.53 \pm 0.39/1.37 \pm 1.20$
$\frac{\Delta EW_0}{\langle EW_0 \rangle}$	$0.52 \pm 0.50$		$0.17 \pm 0.17$	$0.29 \pm 0.34/0.32 \pm 0.28$

though there are no known Herbig–Haro objects along the 3C111 sightlines; Reipurth 2000). Optical studies have found that strong variations of Na I absorption line profiles over a wide velocity range can stem entirely from local gas. For example, Watson & Meyer (1996) found strong variations in multiple Na I absorption components spanning  $\sim 40$  km s $^{-1}$  in the direction of the binary stars HD32039 and HD32040 (their Figure 1), but these stars are at a distance of only 230 pc, meaning that the absorbing gas must all be at a distance of  $< 230$  pc. Here, it is unclear how many of the observed HI absorption components are associated with the Taurus molecular cloud complex—we lack a reliable distance measurement to the absorbing HI structures in this direction. If we were to assume that they are all associated with Taurus, then the range of density variations would be  $\sim 5$ –2000 cm $^{-3}$  for the features with known column densities.

#### 4.3.2. 3C123

3C123 is also in the direction of the Taurus molecular cloud (Figure 19) and has previously shown evidence for TSAS. Goss et al. (2008) constructed an HI optical depth image of 3C123. They identified strong absorption features at  $v = -20.1$  km s $^{-1}$  and  $v = 4.2$  km s $^{-1}$ . They found that the  $-20.1$  km s $^{-1}$  feature showed almost constant absorption across the source, while there was a marginal change ( $2$ – $3\sigma$ ) in optical depth for the  $4.2$  km s $^{-1}$  component.

Here, we match features at  $-19.9$  and  $-19.3$  km s $^{-1}$  whose Gaussian fitted optical depths are identical

( $\tau_{0,1} = \tau_{0,2} = 0.064$ ). Several Gaussian features are fit at velocities close to 4 km s $^{-1}$ , and Figure 3 confirms that there is indeed significant optical depth variation ( $\gtrsim 20\sigma$ ) at these velocities, probably associated with gas in the Taurus molecular cloud complex. The estimated densities in the direction of 3C123 (Table 3) are high but all have uncertainties  $\gtrsim 100\%$ .

#### 4.3.3. 3C225

Crovisier & Kazes (1980) and Crovisier et al. (1985a) measured HI absorption across 3C225 using the Arecibo Observatory and the Westerbork Synthesis Radio Telescope (WSRT), respectively. They both identified a strong absorption feature at  $\sim 4$  km s $^{-1}$  that varied across the source. This feature is associated with one of the cold HI clouds identified by Verschuur (1969) (“cloud A”; Crovisier et al. 1985b). This cloud has a remarkably high pressure and density ( $P/k \sim 6 \times 10^4$  K cm $^{-3}$  and  $n \sim 3000$  cm $^{-3}$ ; Meyer et al. 2012). Here, a  $4.0$  km s $^{-1}$  feature is fitted to both components, with  $\tau_{0,1} = 0.805$  and  $\tau_{0,2} = 0.774$ . Given its distance and change in column density, we find evidence for large density variations on a scale of  $\sim 100$  AU toward 3C225 ( $\Delta n \sim 4200 \pm 3800$  cm $^{-3}$ ), but the uncertainty on this variation is rather large.

## 5. DISCUSSION

### 5.1. Ubiquity of TSAS

Using highly sensitive HI absorption observations, we find  $> 5\sigma$  HI optical depth variations at a level of  $\gtrsim 0.05$  in the direction of 13 of the 14 component pairs. Our

**Table 3.** Properties of Gaussian features with known distances and known column densities. The distance to the Taurus molecular cloud,  $D = 145^{+12}_{-16}$ , comes from Yan et al. (2019). The distance to the local Leo cloud comes from Peek et al. (2011). Feature with only one velocity indicated are the unmatched features; features with two velocities are the matched features. Some features seen toward 3C111 appear multiple times (for the different pairings, AB, AC, and BC).

Component 1	Component 2	v1 km s <sup>-1</sup>	v2 km s <sup>-1</sup>	$D$ pc	$L$ pc	$\Delta N(\text{HI})$ 10 <sup>20</sup> cm <sup>-2</sup>	$\Delta n$ cm <sup>-3</sup>
3C111A	3C111B	-1.78	-1.74	145	0.085	0.68 ± 0.52	259 ± 199
3C111A	3C111B	1.77	2.09	145	0.085	2.78 ± 0.48	1059 ± 210
3C111A	3C111B	6.05	...	145	0.085	3.02 ± 0.10	1152 ± 117
3C111A	3C111B	-4.72	...	145	0.085	0.38 ± 0.10	144 ± 39
3C111A	3C111B	...	3.69	145	0.085	4.51 ± 0.70	1719 ± 313
3C111A	3C111C	-1.78	-2.15	145	0.059	3.82 ± 0.53	2108 ± 295
3C111A	3C111C	1.77	1.63	145	0.059	3.15 ± 1.43	1740 ± 790
3C111A	3C111C	-4.72	...	145	0.059	0.38 ± 0.10	209 ± 53
3C111B	3C111C	2.09	1.63	145	0.143	5.93 ± 1.41	1341 ± 319
3C111B	3C111C	-1.74	...	145	0.143	3.88 ± 0.42	878 ± 94
3C111B	3C111C	3.69	...	145	0.143	4.51 ± 0.70	1019 ± 157
3C123A	3C123B	5.51	5.50	145	0.015	0.19 ± 0.40	401 ± 848
3C123A	3C123B	5.28	4.94	145	0.015	1.31 ± 1.95	2787 ± 4166
3C123A	3C123B	3.75	4.37	145	0.015	0.28 ± 2.13	599 ± 4543
3C123A	3C123B	1.58	...	145	0.015	0.32 ± 0.23	677 ± 487
3C225A	3C225B	3.97	3.99	17	4 × 10 <sup>-4</sup>	0.05 ± 0.04	4248 ± 3798

sources probe a wide range of environments—peak optical depths toward the 14 component pairs range by more than an order of magnitude (Figure 5). These results suggest that variation of HI optical depth profiles on angular scales from 5'' to 4' may be common. In the several cases where we have a good distance estimates, the HI optical depth variations appear to be associated with TSAS. However, for the majority of observed HI structures, we do not know the distance and therefore cannot determine if these features are overdense and overpressured, as has historically been claimed of TSAS. Our results are consistent with previous sensitive HI absorption studies toward multi-component background sources (Crovisier et al. 1985a; Greisen & Liszt 1986). While our sample size is limited, future large-scale HI absorption observations (e.g. GASKAP; Dickey et al. 2013) will provide excellent samples to establish TSAS's ubiquity and other statistical properties.

The abundance of TSAS is an important yet controversial topic when considering its role in the ISM. For example, SZ18 argued on energetic grounds that TSAS clouds overpressured by a factor of  $\sim 100$  could occupy at most a volume filling factor of roughly  $< (2-7) \times 10^{-4}$ . Larger volume filling factors would have a significant effect on the ISM thermal balance.

Optical studies of absorption variations in the direction of large samples of stars have found that only a few percent of sightlines show the absorption variations characteristic of TSAS at scales  $\lesssim 380$  AU (e.g., Smoker et al. 2011; McEvoy et al. 2015), while such variations are more common at scales  $\gtrsim 480$  AU (e.g., Watson & Meyer 1996; van Loon et al. 2013). Multi-epoch observations of HI absorption against pulsars have also suggested that TSAS is uncommon at scales  $\lesssim 500$  AU, with only a select few sightlines showing significant optical depth variation (e.g., Johnston et al. 2003; Weisberg et al. 2008; Stanimirović et al. 2010).

Brogan et al. (2005) argued that TSAS is ubiquitous, and that non-detections represented a spatial-scale selection effect. According to this interpretation, TSAS searches sampling only scales  $\ll 100$  AU—including multi-epoch absorption studies against pulsars and VLBI absorption studies—lack an adequate dynamic range of spatial scales to have a high probability of detecting TSAS. Moreover, as discussed in Section 1 and Section 3, previous multiple-component studies have found significant variations ( $> 3-5\sigma$ ) along most observed sightlines, especially when reaching an optical depth sensitivity of  $\lesssim 0.01$ . Our results are consistent with these previous multiple-component studies.

Stanimirović et al. (2010) discuss the survival of large versus small TSAS in the context of the Koyama & Inutsuka (2002) simulations, wherein TSAS represents the cold, dense cloudlets formed in thermally unstable regions of a post-shocked layer. These small cloudlets eventually evaporate into the hot ambient medium, but the timescale for this evaporation is highly dependent on the size of the cloudlets—clouds 30 AU in size evaporate in  $10^2$ – $10^3$  yr, while clouds  $10^4$  AU in size evaporate in  $10^5$ – $10^7$  yr (Stanimirović et al. 2010). Multiple-component absorption studies (including this work) typically probe the latter scale. The dramatically longer lifetime of TSAS clouds at this scale may explain why significant HI optical depth variations have been found more commonly in these studies than in multi-epoch HI absorption studies against pulsars. Nevertheless, the sample size of TSAS observations—both at the larger and smaller scales—remains small, so it is unclear if the discrepancy in the observed abundance of TSAS indicates an observational bias or a true physical distinction.

### 5.2. Properties of the Optical Depth Variations

Both methods of measuring optical depth variations—the channel-by-channel variations and the variations in fitted Gaussian features—show that the highest variation is seen along lines of sight with the highest HI optical depths. TSAS appears to be most significant where there is a greater quantity of cold HI. Figure 5 affirms this, indicating that the HI optical depth variations are strongest for sources at lower latitudes and with higher HI column densities (and also higher CNM fractions). As seen by Barlow (1993), Lundgren et al. (2007), and Hacker et al. (2013) in variable narrow quasar absorption lines, we find that the fractional variation is largest for sources with low optical depth (Figure 6), which may simply be a consequence of the low optical depth itself (see Section 3.2 and Lundgren et al. 2007).

We find that both variations in the peak optical depths and variations in the linewidths of fitted features contribute to the overall optical depth variation (Figure 10). Moreover, contrary to the argument presented in Brogan et al. (2005), it appears that the turbulent velocity contribution to the linewidths is non-negligible (Figure 17). To precisely determine the relative contributions of thermal motions and turbulent motions to the changes in linewidths, we await higher resolution emission measurements.

Table 3 is consistent with the interpretation that the HI optical depth variations are caused by dense structures along the line of sight. Under this classical interpretation, we find that the density variations toward structures with known distances are on the or-

der of  $\sim 1000 \text{ cm}^{-3}$ , which is an order of magnitude higher than what is typical in the CNM. At least one of these structures—the local Leo cold cloud, in the direction of 3C225—is known to be highly overpressured ( $P/k \approx 60,000 \text{ K cm}^{-3}$ ; Meyer et al. 2012). However, if the optical depth variations are the result of sheets or filaments, then the densities listed in Table 3 may be overestimated by more than an order of magnitude.

If we assume that optical depth features represent discrete, tiny HI structures, then we find that these structures are likely expanding (Section 4.2.6), but that a majority of them may also be in thermal equilibrium with the surrounding ISM, whether or not they are overpressured (Section 4.2.7).

### 5.3. TSAS and Turbulence

Deshpande et al. (2000) showed that  $\Delta\tau/\tau \propto \Delta n/n$ . This assumes that the optical depth fluctuations are small and that the relationship between temperature fluctuations and density fluctuations does not change with physical scale. However, if the relationship between these fluctuations changes with scale (e.g., small scale perturbations are isobaric while larger scale perturbations are isothermal), then this straightforward relationship no longer holds. We find that the fractional change in HI optical depth depends strongly on the optical depth (Figure 6), which indicates that  $\Delta\tau/\tau$ —and, under Deshpande’s assumptions,  $\Delta n/n$ —has a strong environmental dependence. This suggests that the amplitude of density fluctuations is not universal, as would be the case for the universal interstellar turbulence. Instead, density fluctuations appear stronger at low Galactic latitudes and high HI column densities, consistent with the idea that excess energy injection happens in such environments (SZ18).

The turbulent pressure dominates the thermal pressure for most features (Figure 16). This ratio,  $r$ , does not depend on assumptions about the environment (such as the pressure and density, which are still controversial for TSAS). Nevertheless, the magnitude of HI optical depth variation does not appear to be strongly correlated with turbulence (Figure 15). Moreover, Figure 17 indicates that TSAS structures are not pressure confined (following the argument outlined in SZ18 that the turbulent velocity in pressure confined structures should exceed the rms velocity by a factor of  $> 10$ ). Instead, these structures must be transient, be confined by some other mechanism, or be near pressure equilibrium with their surroundings. It is possible, though, that turbulent motions contribute to the the optical depth variation by altering the linewidths of HI structures (see Section 5.2).

### 5.4. Future work

We have found strong evidence that TSAS is correlated with the total quantity of cold HI gas, investigated the role of turbulence in producing TSAS, and estimated TSAS densities for a handful of sightlines, but a number of important questions about the formation and role of TSAS remain.

For example, a geometric understanding of the variable HI structures is still unclear, i.e., are they sheets or filaments as suggested by Heiles (1997), large scale structures as suggested by Deshpande (2000), true tiny dense structures, or none of the above? Obtaining HI optical depth maps, as in Deshpande et al. (2000) and Roy et al. (2012), can constrain the slope of the optical depth power spectrum in different environments, testing the Deshpande (2000) hypothesis. It is particularly important to probe the intermediate scales not covered by either of those experiments. If the hypothesis is correct, then TSAS densities (e.g., Table 3) may be overestimated by over an order of magnitude.

Crovisier et al. (1985a) showed that the change in central velocity of the Gaussian features between adjacent lines of sight could be used as a proxy for the velocity dispersion of the absorbing HI structures ( $\Delta v_0 = |v_{0,1} - v_{0,2}| \sim \sigma_v$ ). If the distances to the HI structures are known, this dispersion can be measured as a function of linear separation,  $L$ , and thereby indicate the source(s) of turbulence (e.g., Larson 1979) associated with tiny scale structures. Here, we only have 9 features for which we know  $\Delta v_0$  and  $L$ . The scatter in  $\Delta v_0$  versus  $L$  is far too large to make a strong statement about the source of turbulence.

The role of temperature in explaining the observed optical depth variation remains unconstrained. Hennebelle & Audit (2007) and Inoue & Inutsuka (2012) showed that steep temperature gradients can form on the outskirts of sub-parsec scale CNM HI clumps that collapse in thermally unstable regions of the WNM. Dramatic temperature variation could alter the linewidth of a given feature, leading to variation in the observed HI optical depth spectrum. Although we have more precise estimates of  $T_S$  than previous TSAS searches, which have generally assumed some (constant) value of  $T_S$  of  $\sim 50$  K, we still lack independent measurements of  $T_S$  across each component pair, and so cannot reliably measure the temperature variation. Higher angular resolution HI emission observations are needed to investigate the question of whether  $T_S$  changes significantly between multiple components (Section 4.2.5).

The above considerations also demonstrate the need for high resolution, non-isothermal numerical models of the formation of tiny scale HI structure. Koyama & Inutsuka (2002), Hennebelle & Audit (2007), and Inoue &

Inutsuka (2012), for example, have shown that the fragmentation of warm HI into cold, dense structures with TSAS-like properties can occur as the result of shock compression and thermal instability. But a detailed description of these structures' turbulent properties, thermal properties, and overall abundance is needed to compare to TSAS observed in HI absorption experiments. It is especially important to probe a range of scales, including the  $\lesssim 100$  AU scale, which is smaller than what was probed by any of the above experiments. Inoue & Inutsuka (2012), the only of those experiments that modeled the flow of HI in three dimensions, reached a spatial resolution of  $\sim 0.02$  pc.

Finally, complementary observations of TSAS in molecular lines at millimeter wavelengths could be used to better understand the environments associated with TSAS by further constraining TSAS densities and assessing the importance of TSAS for interstellar chemistry. Such observations can also test for shocks in the direction of TSAS using tracers such as SiO (e.g., Martín-Pintado et al. 1997; Louvet et al. 2016) or HNCO (e.g., Zinchenko et al. 2000; Rodríguez-Fernández et al. 2010; Kelly et al. 2017).

## 6. CONCLUSIONS

We have used HI absorption spectra toward multiple-component background sources from the 21-SPONGE survey (Murray et al. 2018) and the Millennium Survey (Heiles & Troland 2003a,b) to probe AU-scale atomic structure in the Milky Way. We measured changes in both the integrated properties of the HI optical depth spectra and the Gaussian components fit to the optical depth spectra between component pairs. Our main results can be summarized as follows.

- In 13/14 pairs of HI absorption spectra, the HI optical depth varies by at least  $\sim 0.05$  on angular scales non-continuously spanning from  $5''$  to  $4'$ . This suggests that this level of variation may be common in the ISM.
- The HI optical depth variations are strongest for lines of sight probing a higher HI column density and higher CNM fraction.
- The highest fractional variations in HI optical depth occur for lines of sight with the lowest optical depth, as seen in studies of narrow quasar absorption lines in other galaxies (Barlow 1993; Lundgren et al. 2007; Hacker et al. 2013).

- From the variations in the properties of the fitted Gaussian components, we find evidence that both changes in the peak HI optical depth and the linewidth of HI features contribute to the observed optical depth variation, while the central velocity of Gaussian features does not change much.
- Most of the optical depth variation is associated with CNM structures, but there is not a correlation between the level of HI optical depth variation and spin temperature.
- The apparent AU-scale structures do not appear to be turbulently confined, although turbulent broadening is an important component of measured velocity linewidths.
- A majority of the structures we probed have sufficiently high column densities that they can be in thermal equilibrium with the rest of the ISM despite being overpressured.
- Under a simple geometric assumption, structures for which we can estimate the density appear to be overdense by at least an order of magnitude (e.g., SZ18).

Future analogous studies at molecular wavelengths can determine if the observed AU-scale structures are associated with shocks. Higher resolution emission measurements can both assess the role of temperature variation in producing dramatic changes in HI optical depth and also quantify the relative importance of thermal mo-

tions and turbulent motions in changing the linewidths of HI absorption features. An expanded sample size can be used to better constrain the statistical properties of TSAS in the Milky Way. Finally, we stress the need for high resolution models to investigate the formation of HI structures on tiny scales and compare to observations.

#### ACKNOWLEDGMENTS

S.S. acknowledges the support by the Vilas funding provided by the University of Wisconsin, and the John Simon Guggenheim fellowship. This research was partially supported by the Munich Institute for Astro- and Particle Physics (MIAPP) which is funded by the Deutsche Forschungsgemeinschaft (DFG, German Research Foundation) under Germany's Excellence Strategy - EXC-2094-390783311. D.R. thanks Trey V. Wenger for helpful conversations regarding the kinematic distance estimates to the sources in this study. We thank the anonymous referee for constructive comments. 21-SPONGE data were obtained by the Arecibo Observatory and the Karl G. Jansky Very Large Array (VLA). The Millennium survey data were obtained by the Arecibo Observatory. The Arecibo Observatory is operated by SRI International under a cooperative agreement with the National Science Foundation (AST-1100968), and in alliance with Ana G. Méndez-Universidad Metropolitana, and the Universities Space Research Association. The National Radio Astronomy Observatory is a facility of the National Science Foundation operated under cooperative agreement by Associated Universities, Inc. This research made use of TM-BIDL (Bania et al. 2016). This research made use of Astropy,<sup>3</sup> a community-developed core Python package for Astronomy (Astropy Collaboration et al. 2013; Price-Whelan et al. 2018).

#### REFERENCES

- Astropy Collaboration, Robitaille, T. P., Tollerud, E. J., et al. 2013, *A&A*, 558, A33, doi: [10.1051/0004-6361/201322068](https://doi.org/10.1051/0004-6361/201322068)
- Baker, P. L., & Burton, W. B. 1975, *ApJ*, 198, 281, doi: [10.1086/153605](https://doi.org/10.1086/153605)
- Bania, T., Wenger, T., Balsler, D., & Anderson, L. 2016, TMBIDL: Single dish radio astronomy data reduction package. <http://ascl.net/1605.005>
- Barlow, T. A. 1993, PhD thesis, California University
- Brogan, C. L., Zauderer, B. A., Lazio, T. J., et al. 2005, *AJ*, 130, 698, doi: [10.1086/431736](https://doi.org/10.1086/431736)
- Crovisier, J. 1978, *A&A*, 70, 43
- Crovisier, J., Dickey, J. M., & Kazes, I. 1985a, *A&A*, 146, 223
- . 1985b, *A&A*, 149, 209
- Crovisier, J., & Kazes, I. 1980, *A&A*, 88, 329
- Dame, T. M., Hartmann, D., & Thaddeus, P. 2001, *ApJ*, 547, 792, doi: [10.1086/318388](https://doi.org/10.1086/318388)
- Deshpande, A. A. 2000, *MNRAS*, 317, 199, doi: [10.1046/j.1365-8711.2000.03631.x](https://doi.org/10.1046/j.1365-8711.2000.03631.x)
- Deshpande, A. A., Dwarkanath, K. S., & Goss, W. M. 2000, *ApJ*, 543, 227, doi: [10.1086/317104](https://doi.org/10.1086/317104)
- Dhawan, V., Goss, W. M., & Rodríguez, L. F. 2000, *ApJ*, 540, 863, doi: [10.1086/309371](https://doi.org/10.1086/309371)

- Diamond, P. J., Goss, W. M., Romney, J. D., et al. 1989, *ApJ*, 347, 302, doi: [10.1086/168119](https://doi.org/10.1086/168119)
- Dickey, J. M. 1979, *ApJ*, 233, 558, doi: [10.1086/157416](https://doi.org/10.1086/157416)
- Dickey, J. M., & Terzian, Y. 1978, *A&A*, 70, 415
- Dickey, J. M., McClure-Griffiths, N., Gibson, S. J., et al. 2013, *PASA*, 30, e003, doi: [10.1017/pasa.2012.003](https://doi.org/10.1017/pasa.2012.003)
- Dirks, C., & Meyer, D. M. 2016, *ApJ*, 819, 45, doi: [10.3847/0004-637X/819/1/45](https://doi.org/10.3847/0004-637X/819/1/45)
- Faison, M. D., & Goss, W. M. 2001, *AJ*, 121, 2706, doi: [10.1086/320369](https://doi.org/10.1086/320369)
- Frail, D. A., Weisberg, J. M., Cordes, J. M., & Mathers, C. 1994, *ApJ*, 436, 144, doi: [10.1086/174888](https://doi.org/10.1086/174888)
- Goss, W. M., Richards, A. M. S., Muxlow, T. W. B., & Thomasson, P. 2008, *MNRAS*, 388, 165, doi: [10.1111/j.1365-2966.2008.13300.x](https://doi.org/10.1111/j.1365-2966.2008.13300.x)
- Greisen, E. W., & Liszt, H. S. 1986, *ApJ*, 303, 702, doi: [10.1086/164118](https://doi.org/10.1086/164118)
- Hacker, T. L., Brunner, R. J., Lundgren, B. F., & York, D. G. 2013, *MNRAS*, 434, 163, doi: [10.1093/mnras/stt1022](https://doi.org/10.1093/mnras/stt1022)
- Heiles, C. 1997, *ApJ*, 481, 193, doi: [10.1086/304033](https://doi.org/10.1086/304033)
- Heiles, C., & Troland, T. H. 2003a, *ApJS*, 145, 329, doi: [10.1086/367785](https://doi.org/10.1086/367785)
- . 2003b, *ApJ*, 586, 1067, doi: [10.1086/367828](https://doi.org/10.1086/367828)
- Heiles, C. E. 2000, in *Radio interferometry : the saga and the science*, ed. D. G. Finley & W. M. Goss, 7
- Hennabelle, P., & Audit, E. 2007, *A&A*, 465, 431, doi: [10.1051/0004-6361:20066139](https://doi.org/10.1051/0004-6361:20066139)
- HI4PI Collaboration, Ben Bekhti, N., Flöer, L., et al. 2016, *A&A*, 594, A116, doi: [10.1051/0004-6361/201629178](https://doi.org/10.1051/0004-6361/201629178)
- Inoue, T., & Inutsuka, S.-i. 2012, *ApJ*, 759, 35, doi: [10.1088/0004-637X/759/1/35](https://doi.org/10.1088/0004-637X/759/1/35)
- Johnston, S., Koribalski, B., Wilson, W., & Walker, M. 2003, *MNRAS*, 341, 941, doi: [10.1046/j.1365-8711.2003.06468.x](https://doi.org/10.1046/j.1365-8711.2003.06468.x)
- Kameswara Rao, N., Lambert, D. L., Reddy, A. B. S., et al. 2017, *MNRAS*, 467, 1186, doi: [10.1093/mnras/stx139](https://doi.org/10.1093/mnras/stx139)
- Kelly, G., Viti, S., García-Burillo, S., et al. 2017, *A&A*, 597, A11, doi: [10.1051/0004-6361/201628946](https://doi.org/10.1051/0004-6361/201628946)
- Kim, C.-G., Ostriker, E. C., & Kim, W.-T. 2014, *ApJ*, 786, 64, doi: [10.1088/0004-637X/786/1/64](https://doi.org/10.1088/0004-637X/786/1/64)
- Koyama, H., & Inutsuka, S.-i. 2002, *ApJL*, 564, L97, doi: [10.1086/338978](https://doi.org/10.1086/338978)
- Larson, R. B. 1979, *MNRAS*, 186, 479, doi: [10.1093/mnras/186.3.479](https://doi.org/10.1093/mnras/186.3.479)
- Lazio, T. J. W., Brogan, C. L., Goss, W. M., & Stanimirović, S. 2009, *AJ*, 137, 4526, doi: [10.1088/0004-6256/137/5/4526](https://doi.org/10.1088/0004-6256/137/5/4526)
- Lindner, R. R., Vera-Ciro, C., Murray, C. E., et al. 2015, *AJ*, 149, 138, doi: [10.1088/0004-6256/149/4/138](https://doi.org/10.1088/0004-6256/149/4/138)
- Louvet, F., Motte, F., Gusdorf, A., et al. 2016, *A&A*, 595, A122, doi: [10.1051/0004-6361/201629077](https://doi.org/10.1051/0004-6361/201629077)
- Lundgren, B. F., Wilhite, B. C., Brunner, R. J., et al. 2007, *ApJ*, 656, 73, doi: [10.1086/510202](https://doi.org/10.1086/510202)
- Marscher, A. P., Moore, E. M., & Bania, T. M. 1993, *ApJL*, 419, L101, doi: [10.1086/187147](https://doi.org/10.1086/187147)
- Martín-Pintado, J., de Vicente, P., Fuente, A., & Planesas, P. 1997, *ApJ*, 482, L45, doi: [10.1086/310691](https://doi.org/10.1086/310691)
- McEvoy, C. M., Smoker, J. V., Dufton, P. L., et al. 2015, *MNRAS*, 451, 1396, doi: [10.1093/mnras/stv945](https://doi.org/10.1093/mnras/stv945)
- McKee, C. F., & Zweibel, E. G. 1992, *ApJ*, 399, 551, doi: [10.1086/171946](https://doi.org/10.1086/171946)
- Meyer, D. M., Dirks, C., & Lauroesch, J. T. 2015, in *American Astronomical Society Meeting Abstracts*, Vol. 225, American Astronomical Society Meeting Abstracts #225, 141.23
- Meyer, D. M., Lauroesch, J. T., Peek, J. E. G., & Heiles, C. 2012, *ApJ*, 752, 119, doi: [10.1088/0004-637X/752/2/119](https://doi.org/10.1088/0004-637X/752/2/119)
- Minter, A. H., Balser, D. S., & Kartaltepe, J. S. 2005, *ApJ*, 631, 376, doi: [10.1086/432367](https://doi.org/10.1086/432367)
- Moore, E. M., & Marscher, A. P. 1995, *ApJ*, 452, 671, doi: [10.1086/176338](https://doi.org/10.1086/176338)
- Murray, C. E., Stanimirović, S., Goss, W. M., et al. 2018, *ApJS*, 238, 14, doi: [10.3847/1538-4365/aad81a](https://doi.org/10.3847/1538-4365/aad81a)
- Murray, C. E., Stanimirović, S., Kim, C.-G., et al. 2017, *ApJ*, 837, 55, doi: [10.3847/1538-4357/aa5d12](https://doi.org/10.3847/1538-4357/aa5d12)
- Murray, C. E., Stanimirović, S., Goss, W. M., et al. 2015, *ApJ*, 804, 89, doi: [10.1088/0004-637X/804/2/89](https://doi.org/10.1088/0004-637X/804/2/89)
- Peek, J. E. G., Heiles, C., Peek, K. M. G., Meyer, D. M., & Lauroesch, J. T. 2011, *ApJ*, 735, 129, doi: [10.1088/0004-637X/735/2/129](https://doi.org/10.1088/0004-637X/735/2/129)
- Planck Collaboration, Ade, P. A. R., Aghanim, N., et al. 2014, *A&A*, 571, A13, doi: [10.1051/0004-6361/201321553](https://doi.org/10.1051/0004-6361/201321553)
- Price-Whelan, A. M., Sipőcz, B. M., Günther, H. M., et al. 2018, *AJ*, 156, 123, doi: [10.3847/1538-3881/aabc4f](https://doi.org/10.3847/1538-3881/aabc4f)
- Ray, A., & Loeb, A. 2017, *ApJ*, 836, 135, doi: [10.3847/1538-4357/aa5b7d](https://doi.org/10.3847/1538-4357/aa5b7d)
- Reipurth, B. 2000, *vCat*, V/104
- Rodríguez-Fernández, N. J., Tafalla, M., Gueth, F., & Bachiller, R. 2010, *A&A*, 516, A98, doi: [10.1051/0004-6361/201013997](https://doi.org/10.1051/0004-6361/201013997)
- Roy, N., Minter, A. H., Goss, W. M., Brogan, C. L., & Lazio, T. J. W. 2012, *ApJ*, 749, 144, doi: [10.1088/0004-637X/749/2/144](https://doi.org/10.1088/0004-637X/749/2/144)
- Smith, K. T., Fossey, S. J., Cordiner, M. A., et al. 2013, *MNRAS*, 429, 939, doi: [10.1093/mnras/sts310](https://doi.org/10.1093/mnras/sts310)
- Smoker, J. V., Bagnulo, S., Cabanac, R., et al. 2011, *MNRAS*, 414, 59, doi: [10.1111/j.1365-2966.2011.17987.x](https://doi.org/10.1111/j.1365-2966.2011.17987.x)

- Stanimirović, S., Weisberg, J. M., Pei, Z., Tuttle, K., & Green, J. T. 2010, *ApJ*, 720, 415, doi: [10.1088/0004-637X/720/1/415](https://doi.org/10.1088/0004-637X/720/1/415)
- Stanimirović, S., & Zweibel, E. G. 2018, *ARA&A*, 56, 489, doi: [10.1146/annurev-astro-081817-051810](https://doi.org/10.1146/annurev-astro-081817-051810)
- Thoraval, S., Boisse, P., & Stark, R. 1996, *A&A*, 312, 973
- Ungerechts, H., & Thaddeus, P. 1987, *ApJS*, 63, 645, doi: [10.1086/191176](https://doi.org/10.1086/191176)
- van Loon, J. T., Bailey, M., Tatton, B. L., et al. 2013, *A&A*, 550, A108, doi: [10.1051/0004-6361/201220210](https://doi.org/10.1051/0004-6361/201220210)
- Verschuur, G. L. 1969, *ApL*, 4, 85
- Watson, J. K., & Meyer, D. M. 1996, *ApJL*, 473, L127, doi: [10.1086/310410](https://doi.org/10.1086/310410)
- Weisberg, J. M., Stanimirović, S., Xilouris, K., et al. 2008, *ApJ*, 674, 286, doi: [10.1086/523345](https://doi.org/10.1086/523345)
- Wenger, T. V., Balsaer, D. S., Anderson, L. D., & Bania, T. M. 2018, *ApJ*, 856, 52, doi: [10.3847/1538-4357/aaec8](https://doi.org/10.3847/1538-4357/aaec8)
- Wolfire, M. G., McKee, C. F., Hollenbach, D., & Tielens, A. G. G. M. 2003, *ApJ*, 587, 278, doi: [10.1086/368016](https://doi.org/10.1086/368016)
- Yan, Q.-Z., Zhang, B., Xu, Y., et al. 2019, *A&A*, 624, A6, doi: [10.1051/0004-6361/201834337](https://doi.org/10.1051/0004-6361/201834337)
- Zinchenko, I., Henkel, C., & Mao, R. Q. 2000, *A&A*, 361, 1079. <https://arxiv.org/abs/astro-ph/0007095>
- Zweibel, E. G. 2006, Presentation at Small Ionized and Neutral Structures in the Diffuse Interstellar Medium. [http://www.astro.wisc.edu/~sstanimi/Tiny/SINS\\_Talks1/zweibel1.pdf](http://www.astro.wisc.edu/~sstanimi/Tiny/SINS_Talks1/zweibel1.pdf)



**Table 4.** Summary of Gaussian features fit to the HI absorption spectra from Murray et al. (2018) and Heiles & Troland (2003a). **Column 1:** name of the multiple-component background source; **Column 2:** label of the component in each row; **Column 3:** central velocity of the Gaussian feature; **Column 4:** peak optical depth of the Gaussian feature; **Column 5:** FWHM of the Gaussian feature; **Column 6:** estimated spin temperature of the HI structure; **Column 7:** estimated column density of the HI structure ( $N(\text{HI}) = 1.064 \times 1.823 \times 10^{18} \text{ cm}^{-2}/\text{K km s}^{-1} \times \tau_0 \times b_{\text{FWHM}} \times T_S$ ); **Column 8:**  $\delta$  parameter (Equation 3) for matched components. Rows for matched features are merged. For Columns 1 and 2, we use the naming conventions from Murray et al. (2018) and Heiles & Troland (2003a) (e.g., A/B versus 1/2 for the labeling of components).

Source	Component	$v_0$ km s <sup>-1</sup>	$\tau_0$	$b_{\text{FWHM}}$ km s <sup>-1</sup>	$T_S$ K	$N(\text{HI})$ 10 <sup>20</sup> cm <sup>-2</sup>	$\langle\delta\rangle$
3C018	A	-9.1 ± 0.0	0.565 ± 0.007	2.46 ± 0.02	17 ± 1	0.48 ± 0.04	0.16
	B	-9.0 ± 0.0	0.524 ± 0.003	2.41 ± 0.01	16 ± 2	0.41 ± 0.06	
	A	-6.2 ± 0.1	0.134 ± 0.003	5.49 ± 0.17	196 ± 5	2.81 ± 0.13	0.24
	B	-6.8 ± 0.0	0.149 ± 0.002	6.16 ± 0.06	162 ± 4	2.89 ± 0.10	
	A	-5.0 ± 0.0	0.084 ± 0.003	1.49 ± 0.06	...	...	
	A	24.4 ± 0.1	0.007 ± 0.003	0.75 ± 0.31	...	...	
3C041	A	-1.4 ± 0.1	0.033 ± 0.001	8.87 ± 0.16	351 ± 7	1.99 ± 0.07	0.02
	B	-1.3 ± 0.1	0.042 ± 0.001	7.14 ± 0.22	150 ± 5	0.87 ± 0.05	
	A	1.8 ± 0.1	0.011 ± 0.002	1.21 ± 0.22	98 ± 16	0.02 ± 0.01	
	A	-30.5 ± 0.0	0.029 ± 0.001	1.75 ± 0.06	...	...	
	B	-10.5 ± 0.1	0.022 ± 0.002	1.65 ± 0.19	14 ± 3	0.01 ± 0.00	
	B	-8.0 ± 0.1	0.023 ± 0.003	0.79 ± 0.13	...	...	
3C111	A	-1.8 ± 0.0	0.790 ± 0.009	3.86 ± 0.13	77 ± 4	4.57 ± 0.31	0.02
	B	-1.7 ± 0.0	0.967 ± 0.020	3.69 ± 0.05	56 ± 5	3.88 ± 0.42	
	A	1.8 ± 0.0	0.643 ± 0.020	3.31 ± 0.10	93 ± 8	3.85 ± 0.38	0.25
	B	2.1 ± 0.0	0.347 ± 0.054	2.72 ± 0.15	58 ± 13	1.07 ± 0.30	
	A	-16.8 ± 0.0	0.322 ± 0.003	2.60 ± 0.03	34 ± 5	0.56 ± 0.10	0.05
	B	-16.8 ± 0.0	0.111 ± 0.002	2.69 ± 0.06	30 ± 5	0.17 ± 0.03	
	A	8.4 ± 0.0	0.069 ± 0.004	1.27 ± 0.08	...	...	0.57
	B	8.0 ± 0.0	0.212 ± 0.005	2.07 ± 0.04	...	...	
	A	-8.3 ± 0.0	0.114 ± 0.006	2.09 ± 0.13	...	...	0.03
	B	-8.3 ± 0.0	0.400 ± 0.005	2.81 ± 0.03	14 ± 8	0.32 ± 0.20	
	A	-9.1 ± 0.2	0.172 ± 0.005	8.65 ± 0.31	248 ± 10	7.18 ± 0.46	0.41
	B	-10.8 ± 0.3	0.092 ± 0.002	12.14 ± 0.34	409 ± 10	8.86 ± 0.41	
	A	6.1 ± 0.1	0.232 ± 0.003	5.20 ± 0.13	129 ± 1	3.02 ± 0.10	
	A	-4.7 ± 0.0	0.201 ± 0.011	1.48 ± 0.07	65 ± 15	0.38 ± 0.10	
	A	-21.9 ± 0.1	0.041 ± 0.002	2.57 ± 0.13	131 ± 6	0.27 ± 0.02	
	A	-28.9 ± 0.4	0.013 ± 0.001	5.66 ± 0.97	487 ± 44	0.69 ± 0.15	
	A	-32.4 ± 0.0	0.037 ± 0.003	1.68 ± 0.14	...	...	
	A	6.6 ± 99	0.025 ± 99	0.06 ± 99	...	...	
	B	3.7 ± 0.4	0.342 ± 0.032	5.63 ± 0.36	120 ± 12	4.51 ± 0.70	

**Table 4** continued

Table 4 (continued)

Source	Component	$v_0$ km s <sup>-1</sup>	$\tau_0$	$b_{\text{FWHM}}$ km s <sup>-1</sup>	$T_S$ K	$N(\text{HI})$ 10 <sup>20</sup> cm <sup>-2</sup>	$\langle\delta\rangle$
	B	$-54.8 \pm 0.1$	$0.019 \pm 0.001$	$1.72 \pm 0.15$	$26 \pm 1$	$0.02 \pm 0.00$	
	B	$-2.3 \pm 0.0$	$0.181 \pm 0.006$	$0.78 \pm 0.03$	...	...	
	B	$-51.3 \pm 0.1$	$0.015 \pm 0.001$	$2.16 \pm 0.20$	...	...	
3C111	A	$-1.8 \pm 0.0$	$0.790 \pm 0.009$	$3.86 \pm 0.13$	$77 \pm 4$	$4.57 \pm 0.31$	0.30
	C	$-2.1 \pm 0.0$	$0.816 \pm 0.050$	$2.30 \pm 0.07$	$20 \pm 11$	$0.75 \pm 0.43$	
	A	$6.1 \pm 0.1$	$0.232 \pm 0.003$	$5.20 \pm 0.13$	$129 \pm 1$	$3.02 \pm 0.10$	0.18
	C	$6.3 \pm 0.1$	$0.058 \pm 0.005$	$1.79 \pm 0.16$	...	...	
	A	$-16.8 \pm 0.0$	$0.322 \pm 0.003$	$2.60 \pm 0.03$	$34 \pm 5$	$0.56 \pm 0.10$	0.13
	C	$-16.9 \pm 0.1$	$0.282 \pm 0.045$	$2.06 \pm 0.08$	$20 \pm 4$	$0.23 \pm 0.07$	
	A	$1.8 \pm 0.0$	$0.643 \pm 0.020$	$3.31 \pm 0.10$	$93 \pm 8$	$3.85 \pm 0.38$	0.07
	C	$1.6 \pm 0.4$	$0.456 \pm 0.044$	$7.32 \pm 0.29$	$108 \pm 18$	$7.00 \pm 1.38$	
	A	$-8.3 \pm 0.0$	$0.114 \pm 0.006$	$2.09 \pm 0.13$	...	...	0.08
	C	$-8.4 \pm 0.0$	$0.416 \pm 0.008$	$1.60 \pm 0.03$	...	...	
	A	$-9.1 \pm 0.2$	$0.172 \pm 0.005$	$8.65 \pm 0.31$	$248 \pm 10$	$7.18 \pm 0.46$	0.23
	C	$-8.1 \pm 0.6$	$0.182 \pm 0.011$	$11.25 \pm 0.59$	$118 \pm 28$	$4.69 \pm 1.18$	
	A	$-4.7 \pm 0.0$	$0.201 \pm 0.011$	$1.48 \pm 0.07$	$65 \pm 15$	$0.38 \pm 0.10$	
	A	$-21.9 \pm 0.1$	$0.041 \pm 0.002$	$2.57 \pm 0.13$	$131 \pm 6$	$0.27 \pm 0.02$	
	A	$-28.9 \pm 0.4$	$0.013 \pm 0.001$	$5.66 \pm 0.97$	$487 \pm 44$	$0.69 \pm 0.15$	
	A	$-32.4 \pm 0.0$	$0.037 \pm 0.003$	$1.68 \pm 0.14$	...	...	
	A	$6.6 \pm 99$	$0.025 \pm 99$	$0.06 \pm 99$	...	...	
	A	$8.4 \pm 0.0$	$0.069 \pm 0.004$	$1.27 \pm 0.08$	...	...	
	C	$-15.3 \pm 0.5$	$0.088 \pm 0.027$	$2.54 \pm 0.59$	$90 \pm 34$	$0.39 \pm 0.21$	
	C	$-27.8 \pm 0.1$	$0.029 \pm 0.001$	$2.61 \pm 0.20$	$39 \pm 2$	$0.06 \pm 0.01$	
	C	$-31.4 \pm 0.1$	$0.027 \pm 0.001$	$2.38 \pm 0.19$	$35 \pm 3$	$0.04 \pm 0.01$	
	C	$1.1 \pm 0.0$	$0.584 \pm 0.043$	$2.47 \pm 0.07$	...	...	
	C	$-5.5 \pm 0.0$	$0.211 \pm 0.014$	$1.49 \pm 0.08$	...	...	
3C111	B	$-16.8 \pm 0.0$	$0.111 \pm 0.002$	$2.69 \pm 0.06$	$30 \pm 5$	$0.17 \pm 0.03$	0.18
	C	$-16.9 \pm 0.1$	$0.282 \pm 0.045$	$2.06 \pm 0.08$	$20 \pm 4$	$0.23 \pm 0.07$	
	B	$-8.3 \pm 0.0$	$0.400 \pm 0.005$	$2.81 \pm 0.03$	$14 \pm 8$	$0.32 \pm 0.20$	0.11
	C	$-8.4 \pm 0.0$	$0.416 \pm 0.008$	$1.60 \pm 0.03$	...	...	
	B	$2.1 \pm 0.0$	$0.347 \pm 0.054$	$2.72 \pm 0.15$	$58 \pm 13$	$1.07 \pm 0.30$	0.27
	C	$1.6 \pm 0.4$	$0.456 \pm 0.044$	$7.32 \pm 0.29$	$108 \pm 18$	$7.00 \pm 1.38$	
	B	$-2.3 \pm 0.0$	$0.181 \pm 0.006$	$0.78 \pm 0.03$	...	...	0.31
	C	$-2.1 \pm 0.0$	$0.816 \pm 0.050$	$2.30 \pm 0.07$	$20 \pm 11$	$0.75 \pm 0.43$	
	B	$-10.8 \pm 0.3$	$0.092 \pm 0.002$	$12.14 \pm 0.34$	$409 \pm 10$	$8.86 \pm 0.41$	0.55
	C	$-8.1 \pm 0.6$	$0.182 \pm 0.011$	$11.25 \pm 0.59$	$118 \pm 28$	$4.69 \pm 1.18$	
	B	$-1.7 \pm 0.0$	$0.967 \pm 0.020$	$3.69 \pm 0.05$	$56 \pm 5$	$3.88 \pm 0.42$	
	B	$3.7 \pm 0.4$	$0.342 \pm 0.032$	$5.63 \pm 0.36$	$120 \pm 12$	$4.51 \pm 0.70$	
	B	$-54.8 \pm 0.1$	$0.019 \pm 0.001$	$1.72 \pm 0.15$	$26 \pm 1$	$0.02 \pm 0.00$	

Table 4 continued

Table 4 (continued)

Source	Component	$v_0$ km s <sup>-1</sup>	$\tau_0$	$b_{\text{FWHM}}$ km s <sup>-1</sup>	$T_S$ K	$N(\text{HI})$ 10 <sup>20</sup> cm <sup>-2</sup>	$\langle\delta\rangle$
	B	-51.3 ± 0.1	0.015 ± 0.001	2.16 ± 0.20	...	...	
	B	8.0 ± 0.0	0.212 ± 0.005	2.07 ± 0.04	...	...	
	C	-15.3 ± 0.5	0.088 ± 0.027	2.54 ± 0.59	90 ± 34	0.39 ± 0.21	
	C	-27.8 ± 0.1	0.029 ± 0.001	2.61 ± 0.20	39 ± 2	0.06 ± 0.01	
	C	-31.4 ± 0.1	0.027 ± 0.001	2.38 ± 0.19	35 ± 3	0.04 ± 0.01	
	C	1.1 ± 0.0	0.584 ± 0.043	2.47 ± 0.07	...	...	
	C	-5.5 ± 0.0	0.211 ± 0.014	1.49 ± 0.08	...	...	
	C	6.3 ± 0.1	0.058 ± 0.005	1.79 ± 0.16	...	...	
3C123	A	-19.9 ± 0.0	0.064 ± 0.001	3.13 ± 0.03	26 ± 2	0.10 ± 0.01	0.43
	B	-19.3 ± 0.0	0.064 ± 0.001	3.23 ± 0.04	16 ± 2	0.07 ± 0.01	
	A	20.2 ± 0.1	0.008 ± 0.000	4.05 ± 0.27	124 ± 9	0.08 ± 0.01	0.09
	B	20.1 ± 0.2	0.004 ± 0.001	3.21 ± 0.54	334 ± 52	0.09 ± 0.02	
	A	5.5 ± 0.0	0.628 ± 0.037	1.75 ± 0.03	18 ± 11	0.40 ± 0.24	0.02
	B	5.5 ± 0.0	0.253 ± 0.007	1.47 ± 0.04	81 ± 43	0.59 ± 0.31	
	A	5.3 ± 0.2	0.810 ± 0.071	4.40 ± 0.15	67 ± 25	4.67 ± 1.82	0.12
	B	4.9 ± 0.1	0.042 ± 0.003	10.95 ± 0.33	664 ± 52	5.98 ± 0.69	
	A	3.7 ± 0.1	0.044 ± 0.004	10.13 ± 0.28	619 ± 79	5.36 ± 0.89	0.24
	B	4.4 ± 0.0	1.648 ± 0.005	4.31 ± 0.01	36 ± 14	5.08 ± 1.94	
	A	1.6 ± 0.0	0.379 ± 0.035	2.18 ± 0.05	19 ± 14	0.32 ± 0.23	
	A	3.7 ± 0.0	1.020 ± 0.096	2.28 ± 0.04	...	...	
	B	8.5 ± 0.0	0.064 ± 0.003	1.73 ± 0.09	...	...	
3C225	A	4.0 ± 0.0	0.805 ± 0.001	1.26 ± 0.00	11 ± 2	0.23 ± 0.04	0.03
	B	4.0 ± 0.0	0.774 ± 0.001	1.28 ± 0.00	14 ± 0	0.28 ± 0.01	
	A	-40.2 ± 0.0	0.043 ± 0.002	1.82 ± 0.07	22 ± 0	0.03 ± 0.00	0.13
	B	-40.3 ± 0.0	0.044 ± 0.002	2.00 ± 0.09	18 ± 0	0.03 ± 0.00	
	A	-27.2 ± 0.0	0.048 ± 0.001	2.54 ± 0.04	22 ± 0	0.05 ± 0.00	0.09
	B	-27.3 ± 0.0	0.053 ± 0.001	2.36 ± 0.05	20 ± 0	0.05 ± 0.00	
	A	-37.4 ± 0.2	0.020 ± 0.001	4.76 ± 0.30	60 ± 1	0.11 ± 0.01	0.12
	B	-37.2 ± 0.1	0.023 ± 0.001	4.02 ± 0.31	145 ± 4	0.26 ± 0.02	
	A	-5.2 ± 0.1	0.013 ± 0.000	7.71 ± 0.29	327 ± 11	0.64 ± 0.04	0.10
	B	-5.6 ± 0.2	0.013 ± 0.001	8.32 ± 0.38	458 ± 17	1.00 ± 0.07	
3C245	A	-9.1 ± 0.1	0.010 ± 0.001	5.30 ± 0.26	385 ± 30	0.40 ± 0.05	
	A	-9.8 ± 0.1	0.006 ± 0.001	1.55 ± 0.28	...	...	
3C327.1	A	-0.0 ± 0.0	0.425 ± 0.010	1.91 ± 0.05	63 ± 4	1.00 ± 0.08	0.00
	B	-0.0 ± 0.0	0.359 ± 0.011	1.94 ± 0.07	74 ± 4	1.01 ± 0.08	
	A	2.0 ± 0.0	0.401 ± 0.006	2.17 ± 0.04	69 ± 3	1.18 ± 0.06	0.07
	B	1.9 ± 0.0	0.419 ± 0.008	2.16 ± 0.04	68 ± 3	1.20 ± 0.07	
	A	-2.7 ± 0.1	0.126 ± 0.002	3.36 ± 0.12	140 ± 3	1.16 ± 0.06	0.04
	B	-2.7 ± 0.1	0.118 ± 0.002	3.22 ± 0.13	142 ± 3	1.05 ± 0.05	

Table 4 continued

Table 4 (continued)

Source	Component	$v_0$ km s <sup>-1</sup>	$\tau_0$	$b_{\text{FWHM}}$ km s <sup>-1</sup>	$T_S$ K	$N(\text{HI})$ 10 <sup>20</sup> cm <sup>-2</sup>	$\langle\delta\rangle$
	B	46.1 ± 0.1	0.013 ± 0.002	0.67 ± 0.13	...	...	
3C409	A	4.2 ± 0.0	0.443 ± 0.001	3.19 ± 0.02	64 ± 9	1.77 ± 0.26	0.19
	B	4.0 ± 0.0	0.429 ± 0.003	2.86 ± 0.02	49 ± 9	1.18 ± 0.23	
	A	7.9 ± 0.0	0.332 ± 0.002	3.00 ± 0.03	122 ± 11	2.36 ± 0.22	0.03
	B	8.0 ± 0.0	0.280 ± 0.007	3.01 ± 0.09	120 ± 13	1.97 ± 0.23	
	A	14.6 ± 0.0	0.440 ± 0.008	6.53 ± 0.07	145 ± 20	8.11 ± 1.15	0.03
	B	14.5 ± 0.2	0.106 ± 0.004	13.09 ± 0.19	285 ± 12	7.67 ± 0.45	
	A	13.8 ± 0.0	0.732 ± 0.007	2.15 ± 0.02	13 ± 5	0.41 ± 0.16	0.29
	B	13.6 ± 0.0	0.631 ± 0.081	1.85 ± 0.06	66 ± 22	1.51 ± 0.54	
	A	15.9 ± 0.0	0.735 ± 0.006	1.70 ± 0.01	12 ± 18	0.29 ± 0.44	0.67
	B	15.3 ± 0.1	0.890 ± 0.065	3.01 ± 0.05	47 ± 13	2.45 ± 0.71	
	A	24.3 ± 0.1	0.020 ± 0.001	4.33 ± 0.20	366 ± 39	0.63 ± 0.08	
	A	-53.8 ± 0.1	0.004 ± 0.001	0.64 ± 0.22	...	...	
	B	12.3 ± 0.9	0.193 ± 0.053	3.63 ± 1.24	...	...	
3C410	A	2.7 ± 0.1	0.648 ± 0.023	3.24 ± 0.11	49 ± 14	2.02 ± 0.59	0.21
	B	2.5 ± 0.0	0.426 ± 0.010	2.28 ± 0.06	...	...	
	A	-0.2 ± 0.1	0.613 ± 0.018	3.58 ± 0.11	48 ± 12	2.07 ± 0.54	0.01
	B	-0.2 ± 0.0	0.476 ± 0.005	2.65 ± 0.04	28 ± 2	0.71 ± 0.07	
	A	17.9 ± 0.0	0.186 ± 0.001	3.33 ± 0.05	71 ± 8	0.86 ± 0.11	0.37
	B	18.4 ± 0.0	0.119 ± 0.003	2.53 ± 0.08	...	...	
	A	-30.2 ± 0.1	0.014 ± 0.001	1.46 ± 0.14	15 ± 3	0.01 ± 0.00	0.01
	B	-30.2 ± 0.1	0.019 ± 0.002	1.79 ± 0.27	18 ± 3	0.01 ± 0.00	
	A	25.3 ± 0.1	0.060 ± 0.003	5.25 ± 0.12	69 ± 14	0.43 ± 0.09	0.10
	B	25.2 ± 0.0	0.112 ± 0.002	2.54 ± 0.07	32 ± 3	0.18 ± 0.02	
	A	8.1 ± 0.0	1.864 ± 0.125	1.54 ± 0.03	104 ± 60	5.79 ± 3.39	0.17
	B	8.0 ± 0.0	2.798 ± 0.014	2.19 ± 0.01	18 ± 1	2.15 ± 0.23	
	A	11.1 ± 0.1	0.149 ± 0.081	1.63 ± 0.32	106 ± 45	0.50 ± 0.36	0.23
	B	10.9 ± 0.1	0.430 ± 0.137	1.92 ± 0.12	65 ± 21	1.06 ± 0.48	
	A	11.3 ± 0.4	0.575 ± 0.096	4.39 ± 0.37	111 ± 21	5.46 ± 1.45	0.46
	B	12.7 ± 3.1	0.041 ± 0.017	19.16 ± 1.99	1006 ± 403	15.52 ± 8.97	
	A	7.4 ± 0.1	1.693 ± 0.150	3.16 ± 0.14	70 ± 13	7.33 ± 1.60	
	A	-22.7 ± 0.1	0.020 ± 0.001	3.99 ± 0.20	647 ± 31	0.99 ± 0.08	
	A	-46.5 ± 0.0	0.055 ± 0.001	1.91 ± 0.04	...	...	
	A	-4.8 ± 0.1	0.048 ± 0.002	2.97 ± 0.17	...	...	
	A	24.6 ± 0.0	0.076 ± 0.003	1.79 ± 0.07	...	...	
	B	5.9 ± 0.0	0.292 ± 0.011	1.45 ± 0.04	31 ± 3	0.26 ± 0.03	
	B	5.1 ± 0.3	0.344 ± 0.023	11.43 ± 0.50	153 ± 12	11.71 ± 1.33	
	B	-47.6 ± 0.2	0.021 ± 0.001	5.27 ± 0.42	39 ± 3	0.08 ± 0.01	
	B	12.2 ± 0.4	0.347 ± 0.087	2.57 ± 0.33	...	...	

Table 4 continued

**Table 4** (*continued*)

Source	Component	$v_0$ $\text{km s}^{-1}$	$\tau_0$	$b_{\text{FWHM}}$ $\text{km s}^{-1}$	$T_S$ K	$N(\text{HI})$ $10^{20} \text{ cm}^{-2}$	$\langle\delta\rangle$
3C33	1	$-4.6 \pm 0.1$	$0.034 \pm 0.001$	$9.44 \pm 0.30$	$309 \pm 4$	$1.95 \pm 0.00$	0.15
	2	$-4.2 \pm 0.2$	$0.059 \pm 0.002$	$9.31 \pm 0.42$	$177 \pm 4$	$1.90 \pm 0.00$	
3C75	1	$-10.4 \pm 0.0$	$0.729 \pm 0.014$	$2.06 \pm 0.03$	$34 \pm 4$	$1.02 \pm 0.00$	0.00
	2	$-10.4 \pm 0.0$	$0.647 \pm 0.015$	$2.33 \pm 0.05$	$36 \pm 4$	$1.06 \pm 0.00$	
	1	$-6.1 \pm 0.1$	$0.082 \pm 0.007$	$3.01 \pm 0.30$	$16 \pm 5$	$0.08 \pm 0.00$	0.14
	2	$-6.0 \pm 0.1$	$0.094 \pm 0.009$	$2.34 \pm 0.26$	$34 \pm 4$	$0.15 \pm 0.00$	
	1	$5.0 \pm 0.1$	$0.127 \pm 0.006$	$4.58 \pm 0.22$	$84 \pm 7$	$0.95 \pm 0.00$	0.08
	2	$4.9 \pm 0.1$	$0.139 \pm 0.007$	$4.41 \pm 0.23$	$78 \pm 8$	$0.93 \pm 0.00$	
3C98	1	$-1.2 \pm 0.1$	$0.081 \pm 0.004$	$3.23 \pm 0.18$	$21 \pm 6$	$0.11 \pm 0.00$	0.33
	2	$-1.5 \pm 0.1$	$0.090 \pm 0.004$	$3.16 \pm 0.14$	$58 \pm 5$	$0.33 \pm 0.00$	
	1	$9.4 \pm 0.0$	$0.209 \pm 0.011$	$1.47 \pm 0.09$	$41 \pm 16$	$0.25 \pm 0.00$	0.25
	2	$9.5 \pm 0.0$	$0.203 \pm 0.013$	$1.39 \pm 0.10$	$24 \pm 15$	$0.13 \pm 0.00$	
	1	$9.7 \pm 0.0$	$0.368 \pm 0.008$	$6.07 \pm 0.08$	$114 \pm 5$	$5.00 \pm 0.00$	0.07
	2	$9.6 \pm 0.0$	$0.452 \pm 0.011$	$4.62 \pm 0.06$	$100 \pm 8$	$4.08 \pm 0.00$	
	1	$22.8 \pm 0.3$	$0.028 \pm 0.003$	$5.40 \pm 0.65$	$215 \pm 6$	$0.63 \pm 0.00$	0.22
	2	$22.5 \pm 0.2$	$0.035 \pm 0.003$	$4.56 \pm 0.42$	$165 \pm 6$	$0.52 \pm 0.00$	